Mon. Not. R. Astron. Soc. **340,** 949–968 (2003)

Gas dynamics in the Milky Way: second pattern speed and large-scale morphology

Nicolai Bissantz,[1⋆†] Peter Englmaier[2] and Ortwin Gerhard[1]

[1]*Astronomisches Institut, Universität Basel, Venusstrasse 7, CH-4102 Binningen, Switzerland*
[2]*Max-Planck Institut für extraterrestrische Physik, Garching, Germany*

Accepted 2002 December 11. Received 2002 December 9; in original form 2002 August 19

ABSTRACT

We present new gas flow models for the Milky Way inside the solar circle. We use smoothed particles hydrodynamics (SPH) simulations in gravitational potentials determined from the near-infrared (NIR) luminosity distribution of the bulge and disc, assuming a constant NIR mass-to-light ratio, with an outer halo added in some cases. The luminosity models are based on the *COBE*/DIRBE maps and on clump giant star counts in several bulge fields and include a spiral arm model for the disc.

Gas flows in models that include massive spiral arms clearly match the observed ^{12}CO (l, v) diagram better than if the potential does not include spiral structure. Furthermore, models in which the luminous mass distribution and the gravitational potential of the Milky Way have four spiral arms are better fits to the observed (l, v) diagram than two-armed models.

Besides single-pattern speed models we investigate models with separate pattern speeds for the bar and spiral arms. The most important difference is that in the latter case the gas spiral arms go through the bar corotation region, keeping the gas aligned with the arms there. In the (l, v) plot this results in characteristic regions that appear to be nearly devoid of gas. In single-pattern speed models these regions are filled with gas because the spiral arms dissolve in the bar corotation region.

Comparing with the ^{12}CO data we find evidence for separate pattern speeds in the Milky Way. From a series of models the preferred range for the bar pattern speed is $\Omega_{\rm p} = 60 \pm 5$ Gyr^{-1}, corresponding to corotation at 3.4 ± 0.3 kpc. The spiral pattern speed is less well constrained, but our preferred value is $\Omega_{\rm sp} \approx 20$ Gyr^{-1}. A further series of gas models is computed for different bar angles, using separately determined luminosity models and gravitational potentials in each case. We find acceptable gas models for $20^\circ \lesssim \varphi_{\rm bar} \lesssim 25^\circ$. The model with ($\varphi_{\rm bar} = 20^\circ$, $\Omega_{\rm p} = 60$ Gyr^{-1}, $\Omega_{\rm sp} = 20$ Gyr^{-1}) gives an excellent fit to the spiral arm ridges in the observed (l, v) plot.

Key words: hydrodynamics – ISM: kinematics and dynamics – Galaxy: centre – Galaxy: kinematics and dynamics – Galaxy: structure – galaxies: spiral.

1 INTRODUCTION

Observations of cold gas in the Milky Way (MW) have contributed substantially to our understanding of MW structure. No other tracer is observed in as large a part of the MW as are gas clouds. Longitude-velocity (lv) diagrams (Hartmann & Burton 1997; Dame, Hartmann & Thaddeus 2001) show the distribution of gas velocities as a function of galactic longitude l, integrated over some range in latitude b. By observing the MW in different spectral lines, this gas can be traced at substantially different densities. The largest absolute velocity as a function of l defines the terminal velocity curve (TVC). In an axisymmetric galaxy, the gas at these velocities is found at the 'tangent point' where the line of sight is tangential to a circle around the Galactic Centre. From this the rotation curve can be determined. However, owing to the bar and spiral perturbations in the MW potential, the gas has substantial non-circular velocities, which are most evident in the central 10°–20°, owing to the bar, but also as 'bumps' in the TVC where spiral arm tangents perturb the gas flow by ∼10–20 km s^{-1}. At subTVC velocities, crowding in both position and in velocity produces ridge-like structures in the (l, v)

⋆E-mail: bissantz@math.uni-goettingen.de
†Now at: Institut für Mathematische Stochastik der Universität Göttingen, Lotzestr. 13, 37083 Göttingen, Germany.

diagram. The Galactic spiral arms are visible as straight or curved such ridges.

A number of attempts have been made to model these observations. One group is formed by analytic models of spiral structure. The first exhaustive analytical formulation of a spiral arm theory was developed by Lin & Shu (1964) and applied to the MW by Lin, Yuan & Shu (1969). They proposed a two-armed model with a pitch angle of -6° and a pattern speed for the spiral structure $\Omega_{\rm sp} \approx 13.5$ km s^{-1} kpc^{-1}. Amaral & Lépine (1997) fitted the rotation curve of the MW to an analytic mass model and found a self-consistent solution with a combined two- and four-armed spiral structure. In Lépine, Mishurov & Dedikov (2001) they extended this model to allow for a phase difference between the two- and the four-armed spiral pattern.

The second group, numerical simulations of the Galactic gas flow, also have a long tradition. A recent example is the smoothed particles hydrodynamics (SPH) models of Fux (1999), who evolved a gas disc inside a self-consistent N-body model scaled to the *COBE*/DIRBE K-band map of the MW and the radial velocity dispersion of M giants in Baade's window. The resulting gas flow was transient, but at specific times closely resembled a number of observed arms and clumps in the bar region. Weiner & Sellwood (1999) compared predictions from fluid dynamic simulations for analytic mass densities with the observed outer velocity contours of the H I (l, v) diagram to constrain the pattern speed and bar angle. Englmaier & Gerhard (1999) (hereafter, Paper I) computed gas flows in the gravitational potential of the near-infrared (NIR) luminosity distribution of Binney, Gerhard & Spergel (1997), assuming a constant NIR mass-to-light ratio (M/L). Their best SPH gas flow models reproduced quantitatively a number of observed gas flow features, including the positions of the five main spiral arm tangents at $|l| \leqslant 60^\circ$ and much of the terminal velocity curve.

An important feature of all of these gas flow models is the pattern speed of the non-axisymmetric component. Englmaier & Gerhard found a best pattern speed for the bar $\Omega_{\rm p} \approx 60$ km s^{-1} kpc^{-1}. Weiner & Sellwood derived a bar pattern speed of $\approx$42 km s^{-1} kpc^{-1}, whereas Fux determined $\approx$50 km s^{-1} kpc^{-1} from his models. Dehnen (2000) used resonant features in the *Hipparcos* stellar velocity distribution to argue that the Sun is located just outside the OLR of the exciting quadrupole perturbation, giving a pattern speed of $\approx$51 km s^{-1} kpc^{-1} for solar constants $R_0 = 8$ kpc and $v_0 = 220$ km s^{-1}. For their *spiral structure* model, Amaral & Lépine (1997) and Lépine et al. (2001) found $\Omega_{\rm sp} \approx 20$–$35$ Gyr^{-1}. Fernández, Figueras & Torra (2001) obtained a somewhat higher $\Omega_{\rm sp} \approx 30$ km s^{-1} kpc^{-1} from *Hipparcos* data for OB stars and Cepheids. Debattista, Gerhard & Sevenster (2002) used the Tremaine–Weinberg method on a sample of intermediate age to 8-Gyr old OH/IR-stars in the inner Galactic disc. They found a pattern speed of $59 \pm 5 \pm 10$ (systematic) km s^{-1} kpc^{-1}, which may be driven by the bar in the centre of the MW.

Thus the bar and spiral arms in the MW may not rotate with the same pattern speed. For a fast bar, a single $\Omega_{\rm p}$ would imply that the spiral arms are entirely *outside* their corotation radius. Observations of external galaxies (see, e.g., the Hubble Atlas of Galaxies, Sandage 1961) suggest that galaxies exist with dust lanes on the inner (concave) edges of their spiral arms. For a trailing spiral pattern, these arms would be *inside* their corotation radius. A lower pattern speed for the spiral structure than for the bar would remove this discrepancy. Indeed, Sellwood & Sparke (1988) showed evidence for multiple pattern speeds in their N-body simulations. Rautiainen & Salo (1999) analysed two-dimensional N-body simulations, some of them with a massless, dissipative gas component added. They confirmed the possibility of multiple pattern speeds in self-consistent N-body models of barred galaxies and found a number of possible configurations. These included models with corotating bar and spirals, and models with different pattern speeds. Some of the models in the latter group show evidence for a non-linear mode-coupling (Tagger et al. 1987) between the bar and the spiral pattern, but others show no such evidence. In some of their models there exist separate inner spirals corotating with the bar, and outer spirals that rotate with their own, lower pattern speed. It is therefore tempting to analyse gas flow models of the MW with multiple pattern speeds.

What is the morphology of the MW spiral arms? Most authors infer four spiral arms from tracers, which directly or indirectly measure the gas density, such as molecular clouds, H II regions, pulsars and the galactic magnetic field Georgelin & Georgelin (1976), Sanders, Scoville & Solomon (1985), Caswell & Haynes (1987), Grabelsky et al. (1988), Taylor & Cordes (1993), Vallée (1995); however, Bash (1981) infers a two-armed pattern from the same H II data as used by Georgelin & Georgelin). The problem is that all spiral arm parameters other than the tangent point directions (e.g. Paper I) require distance information. It is also not clear whether all spiral arms seen in the MW gas are present in the old disc. Ortiz & Lépine (1993) constructed a four-armed model that reproduces their star counts in the near-infrared. Drimmel (2000) preferred a two-armed structure from *COBE*/DIRBE K-band data, but a four-armed structure for the dust distribution seen in the 240-μm data. Drimmel & Spergel (2001) project a luminosity model through the 240-μm dust model, to compare with the NIR J- and K-band *COBE*/DIRBE data. Their best model for the stellar distribution is four-armed, but dominated by two spiral arms. Drimmel & Spergel conclude that, if there are four arms in the K-band luminosity distribution, the Sag-Car arm is of reduced strength (by a factor of 2.5).

In this paper we investigate the dynamic effects of the Galactic bar and spiral arms on the gas flow in the Milky Way. We investigate the possibility of different pattern speeds for bar and spiral arms, and the consequences this would have on the observed (l, v) diagrams. Our mass models for the inner Galaxy are based on the NIR luminosity density models of Bissantz & Gerhard (2002) (hereafter, Paper II), which include spiral structure. We use SPH simulations to determine the gas flow in the MW, extending the work presented in Paper I, where eightfold symmetric mass models were used. This paper is organized as follows. In Section 2 we describe the luminosity models, methods and observational data used in this work. In Section 3 we describe our best gas model for the observed ^{12}CO (l, v) diagram. Then we compare models with different pattern speeds (Section 4), bar angles and spiral arm morphology (Section 5) to constrain these parameters and finally give our conclusions in Section 7.

2 GAS DYNAMICAL MODEL

2.1 Mass model of the Milky Way

Here we first describe the adopted model for the distribution of luminous mass in the MW. The model is based on the dust-corrected near-infrared maps of Spergel, Malhotra & Blitz (1995), which they obtained from *COBE*/DIRBE data using a three-dimensional dust model derived from 240-μm observations. From their L-band map we obtained a non-parametric luminosity distribution using the procedure described in Bissantz & Gerhard (2002). Because the non-parametric model only covers the central 5-kpc part of the MW, we used a parametric best-fitting model of the same L-band data to extend the model to larger radii. To convert the luminosity model

to a model for the luminous mass density we assumed a constant L-band mass-to-light ratio.

The model building procedure is described in detail in Paper II. Here we only summarize the most important points. Bissantz & Gerhard estimated the luminosity model iteratively from the L-band data by maximizing a penalized likelihood function. The penalty terms encourage eightfold-symmetry with respect to the three main planes of the bar, as well as smoothness and a prescribed spiral structure model in the disc. The spiral structure term is based on an approximate model for the MW spiral arms from Ortiz & Lépine (1993). The best models resulting from this approach reproduced the dust-corrected *COBE*/DIRBE maps with an rms accuracy of 0.07 mag.

To define the eightfold symmetry penalty term we had to specify the position of the Sun in the MW. Bissantz & Gerhard set the distance of the Sun to the Galactic Centre to $R_0 = 8$ kpc and the vertical distance from the Galactic plane to $z_0 = 14$ pc. These values will be used throughout the present paper as well. The third parameter is the bar angle. Paper II compared photometric models for bar angles $10^\circ \leqslant \varphi_{\rm bar} \leqslant 44^\circ$ and concluded that the best models had bar angles $20^\circ \leqslant \varphi_{\rm bar} \leqslant 25^\circ$.

Paper II also showed that models that include spiral structure are better than models without spiral structure. In particular, because some spiral arm tangent points are evident in the L-band data, such models give a better description of the nearby disc. Also, the inclusion of spiral arms makes a model appear broader on the sky. For given data, this allows the bulge/bar to be more elongated in models with spiral structure. The larger *bulge* elongation in these models makes it possible to reproduce the asymmetries seen in the apparent magnitude distributions of clump giant stars in several bulge fields (Stanek et al. 1994, 1997), for $15^\circ \lesssim \varphi_{\rm bar} \lesssim 30^\circ$. The shape of the bulge/bar in the model with $\varphi_{\rm bar} = 20^\circ$ is approximately 10:3–4:3–4 and its length is approximately 3.5 kpc.

2.2 Gravitational potential

The gravitational force field and potential generated by the distribution of luminous mass were calculated using the multipole expansion method described in Paper I, modified to include phase terms in order to allow for the spiral arm components. The multipole expansion method was used because (i) it allows an independent treatment of disc, bar and spiral arm components, (ii) it works for an arbitrary density distribution and (iii) it does not require detailed boundary conditions as do other methods, since the integrations can easily be extended to infinite radii. The expansion was computed to maximum spherical harmonic orders $l_{\rm max} = 8$ and $m_{\rm max} = 8$. Odd orders were neglected, assuming point symmetry with respect to the centre. Naively, one could interpret the $m = 2$ component as a result of the bar mode and all higher-m modes as a result of spiral arm modes. However, some of the $m = 2$ component beyond the corotation radius of the bar is caused by an $m = 2$ spiral arm mode in the luminosity model (see also Amaral & Lépine 1997).

Since the spatial resolution of the mass models obtained in Paper II is limited by that of the dust-corrected maps of Spergel et al. the central cusp in the density distribution of the MW and potential is incorrectly represented in our multipole expansion model. We attempted to correct for this by modifying the multipole coefficient functions in the centre as in Paper I, replacing the central mass distribution by a power law $\rho^{-1.8}$.

Optionally we add an analytical halo potential

$$\phi_{\rm halo} = \frac{1}{2} V_{\rm inf}^2 \ln (r^2 + a^2),$$

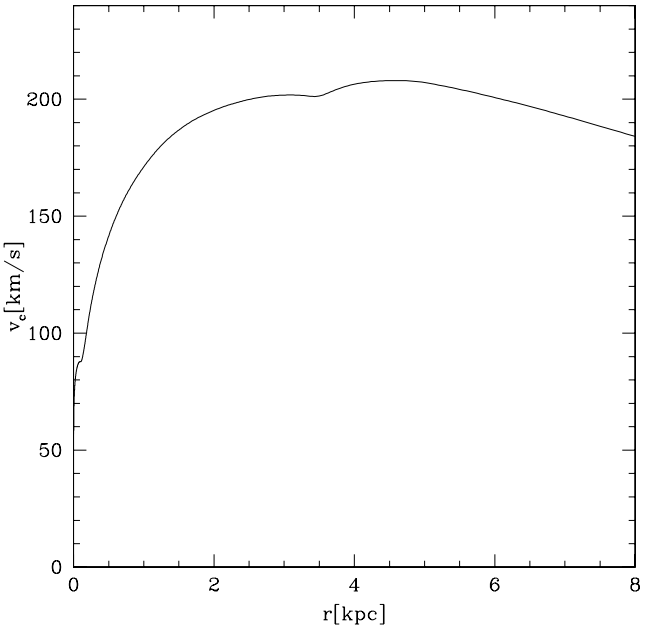

Figure 1. Rotation curve of the standard mass model for bar angle 20°. The velocities have been scaled with the factor ξ determined in Section 3, fitting the observed terminal velocities by the SPH model in $10^\circ < |l| < 50^\circ$.

where $V_{\rm inf}$ is the circular velocity at infinity and a is the core radius. In this paper we use $V_{\rm inf} = 220\,{\rm km\,s^{-1}}$ and determine the core radius such that the model in the potential with halo best fits the TVC near $|l| = 90^\circ$.

Fig. 1 shows the rotation curve derived from the $m = 0$ component of the reference luminosity density model of Paper II (for a bar angle of 20°, with the parametric extension). For brevity, this mass density is called the 'standard mass model' hereafter and the associated gravitational potential the 'standard potential'. Its rotation curve no longer shows a strong bump in the rotation curve of the inner Galaxy as for the models of Paper I (fig. 4 therein). This is because the new luminosity model reproduces light in the spiral arms of the MW significantly better, compared with the density maxima ∼3 kpc down the minor axis of the bar in the earlier models. We note that the spiral arms in the luminosity models used here arbitrarily start at a galactocentric radius of 3.5 kpc. This generates a slight distortion of the rotation curve around this radius.

Fig. 2 shows the quadrupole and octopole terms of the potential, separated into the parts generated by the bar and the parts generated by the spiral arms. All multipoles are normalized by the value of the monopole term at the respective Galactic radius. Note that in this model the bar plays a major role for the non-axisymmetric forces, in particular the quadrupole moment, even beyond where it ends in the mass density.

The multipole representation of the potential is used in the orbital analysis and in the two-dimensional SPH hydrodynamics code, as described in Paper I. The bar and spiral components are both given a constant pattern speed. In most models described below, the bar and spiral arm patterns rotate with different pattern speeds, implying that the mass distribution and potential undergo periodic oscillations; in some models these pattern speeds are equal and the mass distribution is constant in the rotating frame.

Fig. 3 shows a resonance diagram for the standard mass model with the same scaling as in Fig. 1. (The scaling constant is different by $\lesssim$1.5 per cent for models 40 and 60, which have significantly

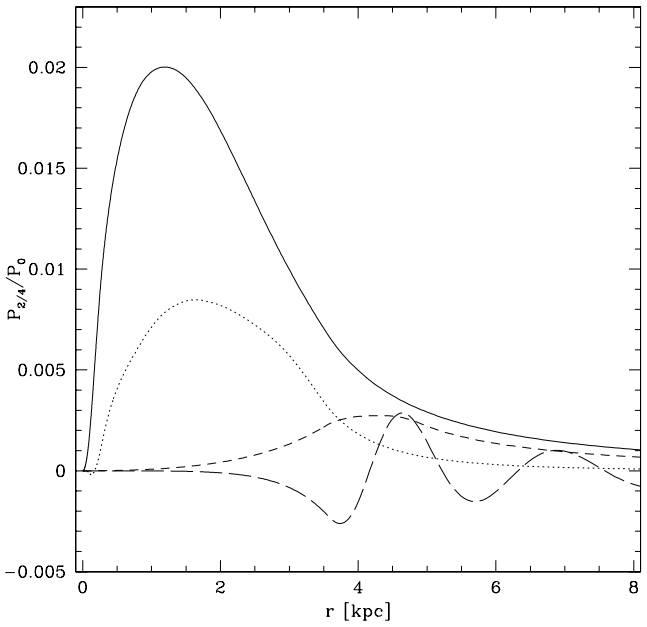

Figure 2. Quadrupole and octopole terms of the standard potential, separated into the part generated by the triaxial bar/bulge in the distribution of luminous mass (full line, $m = 2$; dotted line, $m = 4$), and the part caused by the spiral arms (short dashed, $m = 2$; long dashed, $m = 4$). All multipoles are normalized by the value of the monopole term at the respective Galactic radius.

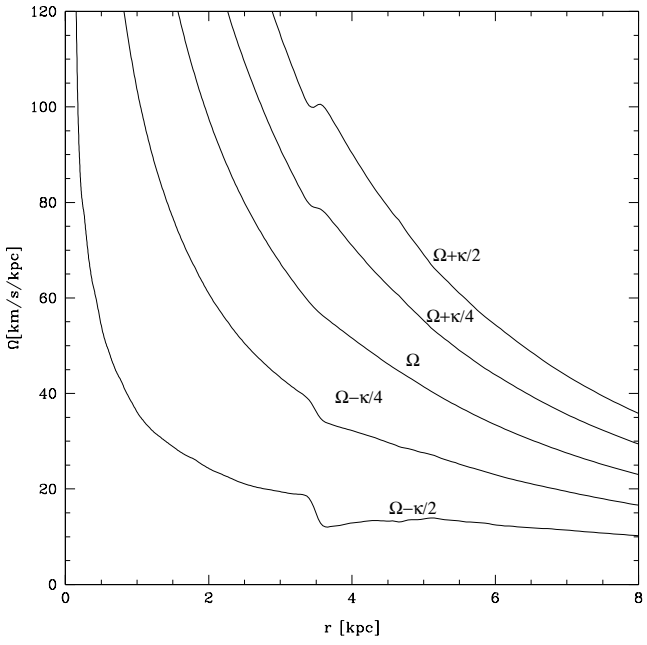

Figure 3. Resonance diagram for the standard mass model, assuming the same velocity scaling as in Fig. 1.

different spiral pattern speeds from our standard model.) We will see below that the preferred bar pattern speed is $\Omega_p = 60$ Gyr^{-1}. Observe from Fig. 3 that in this case the corotation radius of the bar nearly coincides with the inner ultraharmonic resonance of the spiral structure, if this has pattern speed $\Omega_{sp} = 40$ Gyr^{-1}, and with its inner Lindblad resonance, if $\Omega_{sp} = 20$ Gyr^{-1}. Models with these values for the spiral arm pattern speed in conjunction with $\Omega_p = 60$ Gyr^{-1} are particularly interesting to analyse (Tagger et al. 1987) and are discussed below.

2.3 Hydrodynamical method

We use the two-dimensional smoothed particles hydrodynamics code described by Englmaier & Gerhard (1997). The code solves Euler's equation for an isothermal gas with effective speed of sound c_s:

$$\frac{\partial \boldsymbol{v}}{\partial t} + \boldsymbol{v}(\cdot\boldsymbol{\nabla})\boldsymbol{v} = -c_s^2 \frac{\boldsymbol{\nabla}\rho}{\rho} - \boldsymbol{\nabla}\Phi. \quad (1)$$

This approach is based on a result of Cowie (1980). He showed that an isothermal single-fluid description crudely approximates the dynamics of the interstellar medium (ISM). However, here the isothermal speed of sound is not the thermal speed of sound, but an effective speed of sound representing the rms random velocity of the cloud ensemble.

The SPH method has the advantage of allowing for a spatially adaptive resolution length. This is achieved by adjusting the smoothing length h of a particle everywhere such that the number of particles that overlap a given particle is approximately constant. Fluid quantities are approximated by averaging over neighbouring particles. Furthermore, the SPH scheme includes an artificial viscosity to allow for shocks in the simulated gas flow. For further discussion of the method see Englmaier & Gerhard (1997), Paper I and Steinmetz & Müller (1993).

Our SPH models contain 50 000–60 000 particles, except when indicated otherwise. The initial surface density of the models is taken to be constant inside a 8-kpc galactocentric radius.

2.4 Comparison with observational data

Our main tools to compare our gas flow models with observations are the terminal velocity curve and the (l, v) diagram, which shows the radial velocities of gas clouds as a function of galactic longitude. Throughout this paper observed velocities are given with respect to the local standard of rest (LSR). For the distance of the Sun from the Galactic Centre we assume $R_0 = 8$ kpc. The LSR circular velocity is assumed to be $v_0 = 220$ km s^{-1}, consistent with $R_0 = 8$ kpc (Feast & Whitelock 1997; Reid et al. 1999; Backer & Sramek 1999). Note that a 10 per cent change in v_0 is not critical, amounting to radial velocity variations of only $\sim$10 km s^{-1} in the central $l = 45^\circ$ (cf. Paper I).

(l, v) diagrams for our gas flow models are constructed as follows. The LSR observer is specified by the galactocentric radius R_0, the LSR circular velocity V_0 and by the angle φ_{bar} relative to the bar. We first project all particle velocities (v_x, v_y) on to the line-of-sight vector $\boldsymbol{e}_p$ from the LSR observer to the particle, subtracting the component of V_0 in the direction of the particle:

$$v_r = \boldsymbol{e}_p \cdot (v_x, v_y) - v_0 \sin(l). \quad (2)$$

We then construct a two-dimensional binned histogram of the particle distribution in the l–v-plane, with bin size $\approx 0.23^\circ \times 0.7$ km s^{-1}. Finally, we convert this histogram into a grey-scale plot, using a lower surface density cut-off $C_{lv} = 0.5$–1 per cent to enhance the contrast. C_{lv} varies between different models and is selected so as to optimize the visibility of the spiral arm ridges and the terminal velocity envelope.

We compare a model with observations in a two-step process. In the first step, we focus on the terminal velocities, comparing the model TVC with an observed TVC composed from the following

data: H I velocities from Burton & Liszt (1993); H I velocities from Fich, Blitz & Stark (1989), based on data from Westerhout (1957); unpublished 140-ft single-dish H I velocities, kindly provided by Dr B. Burton; northern ^{12}CO velocities from Clemens (1985), including error bars; and southern ^{12}CO velocities from Alvarez, May & Bronfman (1990). The Clemens (1985) data were corrected for internal dispersion (Paper I). The observed velocities, corrected by the respective authors or Paper I to the pre-*Hipparcos* LSR frame, in which the Sun was assumed to move with approximately $u_\odot = -10$ km s^{-1} inwards and $v_\odot = 15$ km s^{-1} in the forward direction of Galactic rotation, are here transformed to the *Hipparcos* LSR frame ($u_\odot = -10$, $v_\odot = 5$ km s^{-1}, Dehnen & Binney 1998), by subtracting $10 \sin l$ km s^{-1}.

A free parameter of our models is the mass-to-light ratio. From the comparison of the model TVC with the observed TVC we determine the best-fitting scaling factor ξ for the model velocities. This parameter ξ, which determines the mass scale of the model, varies by ∼5–10 per cent between all our models. We only use the TVC data for $10^\circ < |l| < 50^\circ$ to determine ξ, because near the centre the resolution of our models is insufficient, and because for $|l| \gtrsim 50^\circ$ the halo contributes significantly (see below). In the fitting we take special care of the location of 'bumps' in the TVC, because these indicate spiral arm tangents. This procedure assumes that the NIR disc and bulge are responsible for all of the observed velocities in the central parts of the MW.

In most models the gravitational potential is time dependent, because the pattern speeds of bar and spirals are different. In this case we select a 'best' snapshot, corresponding to a specific phase and evolutionary age. The value of ξ generally depends slightly on both the model and the evolutionary age of the snapshot.

In the second step we compare the model (l, v) diagram with the observed ^{12}CO (l, v) diagram of Dame et al. (2001) (Fig. 4), using the scaling ξ from the TVC. Important features in the observed (l, v) diagram are the ridges of emission that indicate the location of spiral arms. The white lines drawn in Fig. 4 reproduce approximately the locations of these spiral arm ridges. These lines are then transformed to the *Hipparcos* LSR [Fig. 4 was constructed assuming a solar motion of $|v_\odot| = 20$ km s^{-1} towards $(l, b) = (56.2^\circ, 22.8^\circ)$] and are then overplotted on most model (l, v) diagrams. These observed ridges should be reproduced by a good model of the MW gas flow. The reverse need not always be true, however, because the visibility of a spiral arm ridge in the data may depend on the radial distribution of gas and the geometry of the arm with respect to the line of sight.

In the model (l, v) diagrams we also show molecular cloud observations of Dame et al. (1986) and Bronfman, Nyman & Thaddeus (1989) (symbol '×' in the plots) and H II region observations of Georgelin & Georgelin (1976), Downes et al. (1980) and Caswell & Haynes (1987) (symbol '+'). Most of our models do not contain a halo potential and therefore underestimate the velocities for $|l| \gtrsim 40^\circ$–50°. Thus we omit the molecular cloud and H II observations in these models for $|l| > 40^\circ$. For the sake of clarity we have also left out clouds with less than $10^{5.5}$ M$_\odot$ from the Bronfman et al. data, and clouds in the smallest brightness bin from the Georgelin & Georgelin sample. For a more detailed discussion of these observations see Paper I.

3 BEST-FITTING MODEL FOR THE MILKY WAY

We have investigated a number of gas flow models in the *COBE* potentials of Section 2, for different pattern speeds, bar angles and stellar spiral arm morphologies. The analysis of these model sequences is deferred to Section 4. Here we begin with a description of our best model for the gas dynamics in the MW. This best-fitting model (hereafter called the 'standard model') is based on the

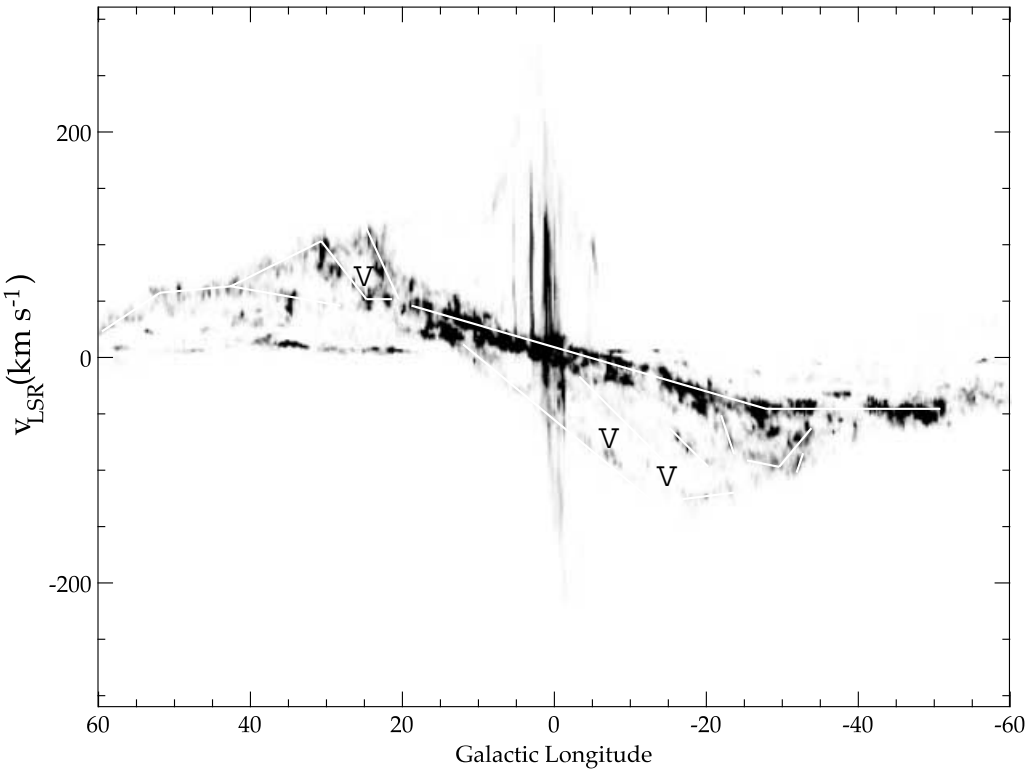

Figure 4. Central part of the ^{12}CO observations of Dame et al. (2001). White lines sketch spiral arm ridges in the data.

standard four-armed $\varphi_{\rm bar} = 20^\circ$ luminosity model (Bissantz & Gerhard 2002, Paper II), as described in Section 2, it is point-symmetric, the bar pattern speed is $\Omega_{\rm p} = 60$ Gyr^{-1}, implying corotation at $R_{\rm cr} \approx 3.4$ kpc and the spiral arm pattern speed is $\Omega_{\rm sp} = 20$ Gyr^{-1}.

The gas distribution of the model is shown in Fig. 5. In this plot the Sun is at $(x, y) = (7.5, 2.7)$ kpc, with $R_0 = 8$ kpc. Both inside and outside corotation there exist four spiral arms that are connected in a complicated way through the corotation region of the bar. Outside corotation the spiral pattern in the gas response consists of a pair of strong arms and a pair of weaker arms.

To compare the model with the gas observations, we scale it to the observed terminal velocity curve in the longitude range $10^\circ \leqslant |l| \leqslant 50^\circ$, using an LSR circular velocity $V_0 = 220$ km s^{-1}. With this scaling the CO TVC is reproduced well by the model (Fig. 6), including most distinct 'bumps' in the observations except that at $l \approx 50^\circ$. Vice versa, the model TVC shows an extra bump at $l \approx -15^\circ$, which is not seen in the data. Presumably the potential in this bar–disc transition region is not accurately modelled – there is little information in the NIR data on the mass distribution in this region. Overall, however, the fall-off with longitude and even the detailed form of the inner disc Galactic TVC are represented well by the model.

In the bulge region, for $|l| \lesssim 10^\circ$, the model velocities are limited by the resolution of the hydrodynamic simulation. We thus do not expect to fit the observed large terminal velocities there, but several other effects may play a role as well. See Section 3.1 below and Englmaier & Gerhard (1999) for a more detailed discussion. Because the gas particles in the numerical simulations flow inwards, however, the velocity structure in the inner 1–1.5 kpc is not of significant relevance for the gas flow and, particularly, for the shock structure in the main spiral arms well outside this region. Only the velocities of the pair of inner arms passing the minor axis of the bar laterally at ≈1 kpc could be somewhat affected. Since the main aim here is to investigate the *large-scale* gas flow and spiral arm morphology, we have therefore not attempted a detailed fit to the inner bulge terminal velocities.

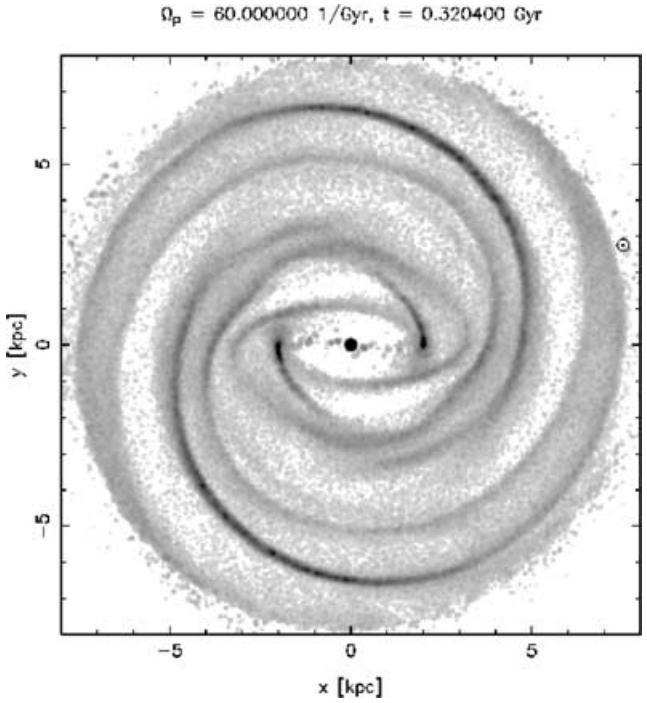

Figure 5. The distribution of gas in the standard gas model at evolutionary age 0.32 Gyr. Note that the initial particle distribution in the simulation ends at $R = 8$ kpc, producing the artificial outer cut-off of the particle disc in the plot. The position of the Sun at $(x, y) \approx (7.5$ kpc, 2.7 kpc) is shown by the $\odot$ symbol.

The standard model does not contain a dark matter halo. For the assumed LSR velocity of $V_0 = 220$ km s^{-1}, its TVC falls below the observed TVC at $|l| \gtrsim 40^\circ$–50°. At $|l| = 90^\circ$ the deficit in the terminal velocity of the model is ≈25 km s^{-1}. This can be corrected by adding a halo potential that generates a rotation velocity $v_{\rm DM} \approx 120$

Table 1. The gas models discussed in this paper.

Model	Potential	$\Omega_{\rm p}$ (Gyr^{-1})	$\Omega_{\rm sp}$ (Gyr^{-1})	Remarks
20	Standard	60	19.6	Standard model
40	Standard	61.4	40.8	
60	Standard	61.4	61.4	
Halo	Standard	60	19.6	Standard model including halo
Bar50	Standard	50	20	
Bar70	Standard	70	20	
Open2	Two-armed, pitch angle similar to standard four-armed model	60	20	
2spi	Two-armed, pitch angle half the value in the standard four-armed model	60	20	
Mix	Similar to four-armed model, but Sag-Car arm and counter-arm are reduced in amplitude	60	20	
Noarms	Standard with spiral perturbation switched off	60	20	
Incl10	Four-armed model, bar angle 10°	60	20	
Incl15	Four-armed model, bar angle 15°	60	20	
Incl25	Four-armed model, bar angle 25°	60	20	
Incl30	Four-armed model, bar angle 30°	60	20	
Strongarms	Standard	60	20	$m \geqslant 2$ multipoles of density outside 3.5 kpc multiplied by 1.5
Tumblingbar		60	20	Standard potential, but the centre of the bar perturbation is not in MW centre

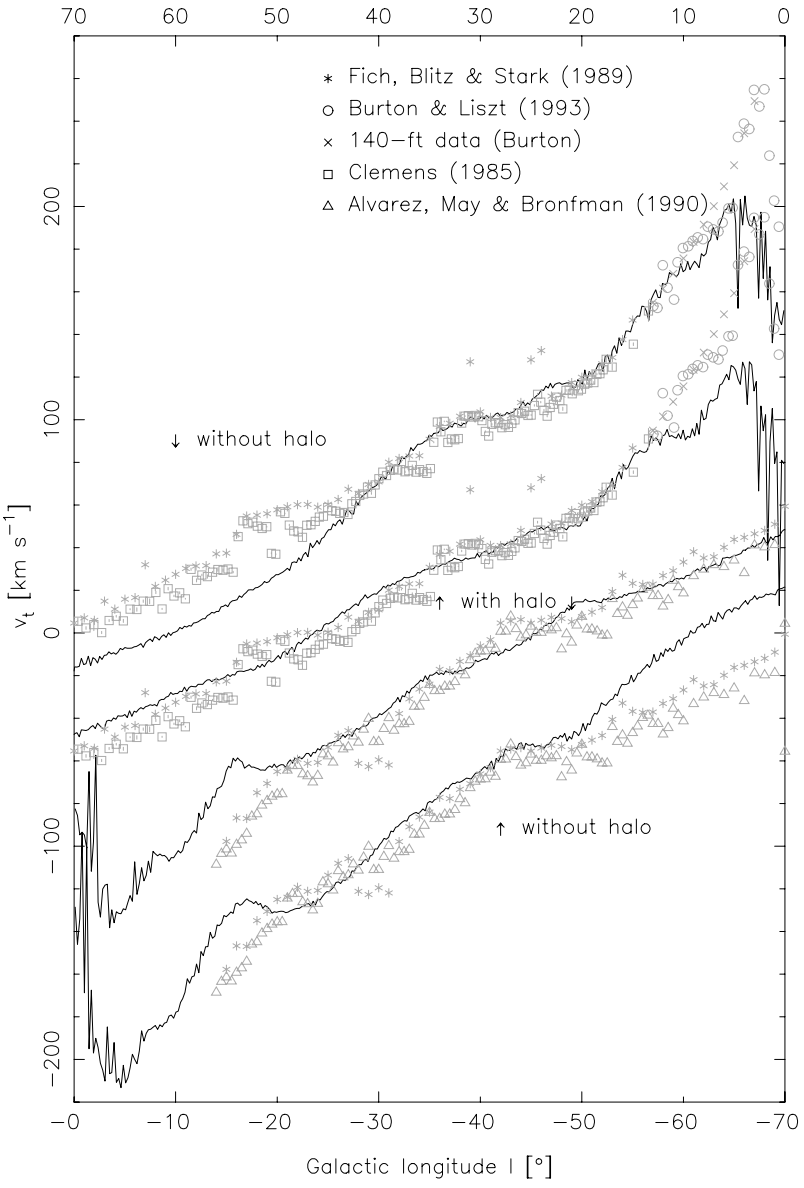

Figure 6. The terminal velocity curve of the standard gas model at evolutionary time 0.32 Gyr (top and bottom curves) and of model halo also at time 0.32 Gyr (middle curves), compared with the H I and CO data. Model velocities have been scaled by a model-dependent factor ξ to best fit the observed terminal velocities for $10^\circ < |l| < 50^\circ$. The observed velocities are corrected to the *Hipparcos* LSR frame as described in Section 2.4. The TVCs of model halo are offset by 60 km s^{-1} for better readability of the diagram.

km s^{-1} near the Sun. We thus constructed a new gas model in a potential that includes a suitable quasi-isothermal dark matter halo, which has circular velocity at infinity $V_{\rm inf} = 220$ km s^{-1} and core radius $a = 10.7$ kpc (there is substantial freedom in these parameter values). The TVC of this model halo is also shown in Fig. 6; its best-fitting scaling factor ξ and mass-to-light ratio is only slightly different from that of the standard model. The model halo fits the shape of the observed TVC out to R_0, but is not quite as good a match to the bumps in the TVC as the standard model. This suggests that the assumed halo model is oversimplified. Note the fact that the constant M/L standard model, a maximum disc model by construction, reproduces the observed terminal velocities inside a galactocentric radius $R \approx 5$ kpc and still accounts for most of the circular velocity near the Sun.

The (l, v) diagram for the standard model is shown in Fig. 7. The dense ridges in this diagram show the locations of the spiral arms. Fig. 11 of Paper II shows the correspondence between the locations of spiral arms in the Galactic plane and in the (l, v) diagram. The model spiral arm ridges in Fig. 7 generally coincide very well with the observed spiral arm ridges. Less good is the correspondence for the 3-kpc arm (again in the bar–disc transition region), which is at too small negative velocities in the model compared with the observations for $l \gtrsim -5^\circ$.

For model halo the lv-plot is shown in Fig. 8, at enhanced contrast to emphasize the spiral arms (see Section 2.4). Compared with the standard model (l, v) diagram (without a halo), significant differences are in the outer spiral tangents near $l \approx \pm 50^\circ$, which are relocated by a few degrees and in the terminal velocities at $|l| \gtrsim \pm$

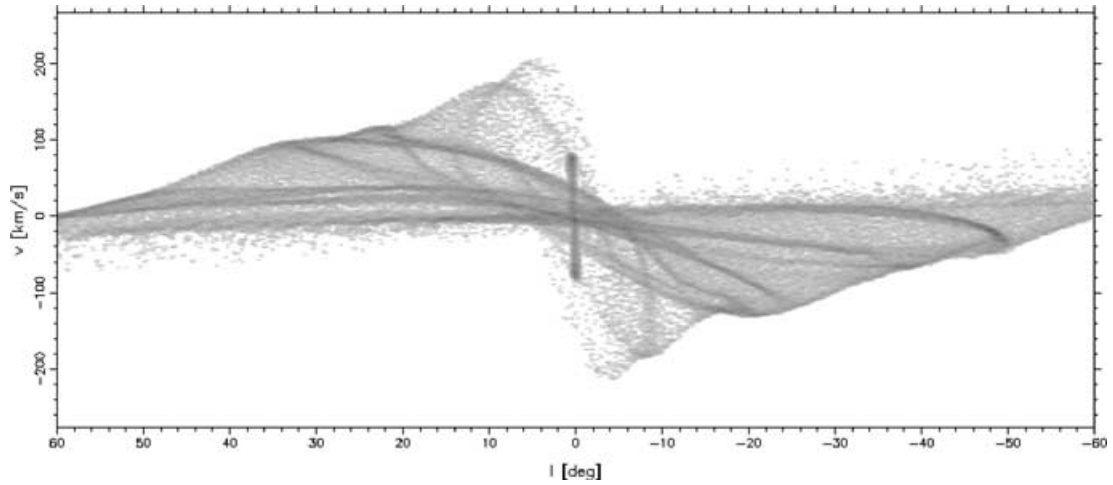

Figure 7. (l, v) diagram for the standard gas model at evolutionary age 0.32 Gyr, for LSR velocity $V_0 = 220$ km s^{-1}. The model velocities are scaled with the factor ξ determined from Fig. 6.

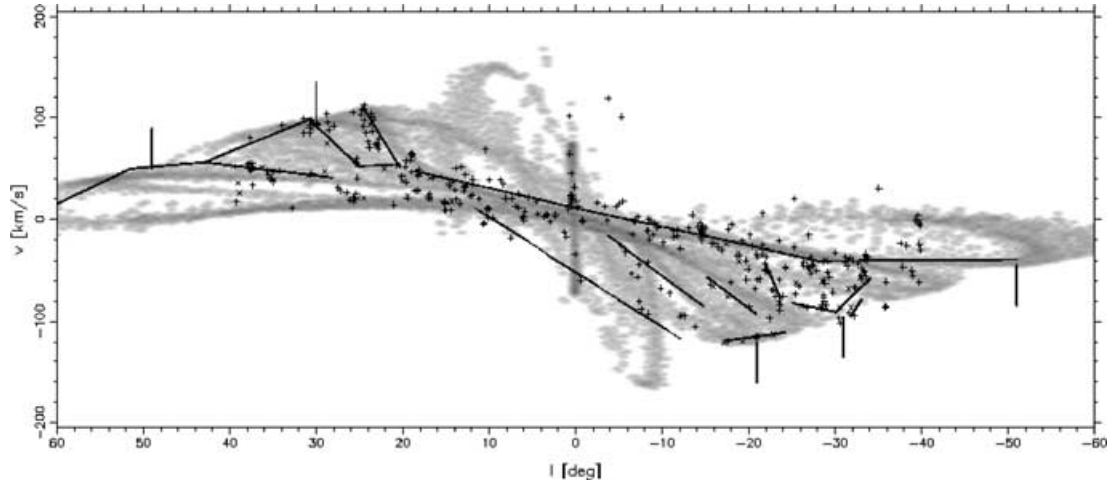

Figure 8. Grey-scale lv-plot for the standard gas model with a dark halo component included in the potential (model halo), at evolutionary age 0.32 Gyr. Particles in regions of low gas surface density (<1 per cent of the maximum surface density) are suppressed to enhance the contrast, mimicking also the bias of the observed distribution of molecular gas and H II regions towards higher densities. Model velocities are scaled such as to fit best the observed terminal velocities in $10^\circ \leqslant |l| \leqslant 50^\circ$ (see Fig. 6); the LSR velocity is 220 km s^{-1}. For comparison with observations, the spiral arm ridge lines from Fig. 4 are overplotted, as are the data for giant molecular clouds from Dame et al. (1986) and Bronfman et al. (1989) ('×' symbols) and for H II regions from Georgelin & Georgelin (1976), Downes et al. (1980) and Caswell & Haynes (1987) ('+' symbols); see Section 2-4. The short vertical lines mark the observed spiral arm tangent directions from Englmaier & Gerhard (1999).

50°. This is a general result: for a number of models discussed later in this paper we have added a suitable halo potential and computed a new gas model, sometimes additionally changing the extent of the initial gas disc in the simulation from the standard 8 kpc to 10 kpc. In all of these cases the only significant change has been that the outer tangent points moved outwards in longitude by $|\Delta l| \lesssim 5^\circ$. Thus we do not include a halo potential in the remaining models discussed below.

Also shown in Fig. 8 are the observed spiral arm ridge lines, tangent points and tracers from Section 2.4. The comparison with the grey-scale plot for the model shows that model halo gives a very good description of the gas kinematics in the disc outside the bar. For many features deviations are less than ∼10 km s^{-1}.

We end this section with showing in Fig. 9 a map of the radial velocities of gas clouds with respect to the LSR for model halo. This map allows one to assess the likely errors made in determining kinematic distances from cloud radial velocities by assuming a circular orbit model.

3.1 Orbits and gas flow in the bulge region

In this section we consider in more detail the gas flow and TVC in the central $|l| \lesssim 10^\circ$. The discussion of the large-scale morphology and pattern speed is continued in Section 4.

We begin with an analysis of closed orbits in the standard potential, including a central cusp in the mass model as described in Section 2.2, and assuming the same values for the pattern speeds as in the standard gas model. The closed orbits are found with a simple shooting algorithm. Despite the intrinsic time dependence of the potential in the bar frame, the closed orbits in the inner kpc remain essentially unperturbed. Fig. 10 shows closed x_2- and x_1-orbits around the so-called 'cusped' orbit, the x_1-orbit where the

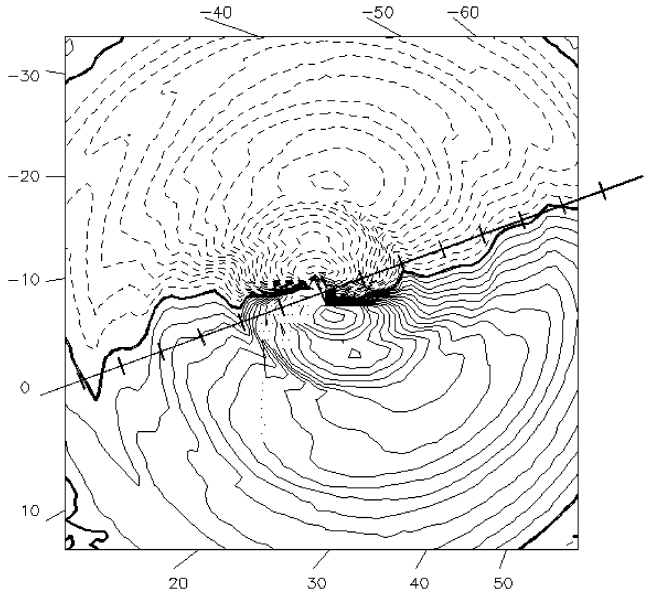

Figure 9. Contours of constant radial velocity for gas clouds in model halo, as seen by an observer moving with the velocity of the LSR. Contours are spaced by 10 km s^{-1}. Dashed contours indicate negative radial velocities, full contours positive radial velocities. Ticks along the full line give distances from the LSR (right end), in kpc along the line of sight through the Galactic Centre. Longitudes as seen from the LSR are indicated on the margin of the plot.

turning points on the major axis of the bar have a cusp shape. Closer to the Galactic Centre the more tightly bound x_1-orbits become self-intersecting and the x_2-orbit family of stable orbits elongated perpendicular to the bar appears. Note that in this potential the outermost x_2-orbits are (nearly) converging on the major axis of the bar, implying that gas clouds on these orbits would collide. This limits the radial extent of *accessible* x_2-orbits for gas clouds in a hydrodynamic flow.

Between the cusped x_1-orbit and the first non-intersecting x_2-orbit there is a region in which no closed orbits suitable for gas flow exist (Fig. 10). Because of this, inflowing gas has to quickly pass this region: the mechanism described by Binney et al. (1991), where gas moving in from the previous x_1-orbits collides with gas on the outermost x_2-orbits, producing a spray that then forms an off-axis shock by hitting the far side of the x_1-orbits, cannot work as well in the potential here because of the lack of suitable outer x_2-orbits. Instead, the main place of dissipation of kinetic energy is likely to be the self-crossing loops of the x_1-orbits inside the cusped orbit, from where the gas moves inwards to hit the x_2-disc further in. This may explain why there is a mostly gas-free gap in the hydrodynamic simulations between the last non-intersecting x_1-orbit and the first accessible x_2-orbit, without any clear off-axis shocks such as those found in other barred galaxy models (e.g. Athanassoula 1992).

How would gas clouds following the closed orbits in our standard model potential compare with the terminal velocity observations? Fig. 11, plotted for a bar angle of 20°, shows that the terminal velocities of the closed x_1-orbits reproduce the observations surprisingly well. The cusped orbit in Fig. 11 is not only at the same longitude as the maximum in the observed TVC (at positive l where we have data), but also appears to account for the decline of the observed terminal velocities at lower l. This is consistent with a gas-free gap between the cusped orbit and the first acceptable x_2-orbit, owing to which no strong leading shocks form such as those observed in other barred galaxies. Episodic infall of gas clouds within the gap region may none the less form transient shocks similar to those observed by Hüttemeister et al. (1998).

The *closed orbits* thus reproduce the observed terminal velocities, but why is there no gas at these velocities in the simulations? Possible explanations are as follows: first, the resolution length of our SPH code, which is dominated by the smoothing length of the SPH particles, may be too large to follow the strongly elongated x_1-orbits near their cusped ends. Also, in the low-density region further in, the relative velocities of neighbouring particles are large, so that the corresponding viscosity may lead to fast infall of SPH particles to the centre. This would depopulate the inner x_1-orbits, where the largest terminal velocities are expected. Indeed, the terminal velocity curve attains larger peak velocities in high-resolution models with some 10^5 particles (the standard gas model has $\approx 6 \times 10^4$ particles), for example the maximum is at $\approx$222 km s^{-1} on the $l > 0°$ side, compared with $\approx$210 km s^{-1} in the standard gas model.

Secondly, the detailed orbit shapes in the inner kpc of the MW depend on the fine structure of the potential there, which is not accurately known, both because of the limited resolution of the underlying NIR data and luminosity model and the difficulty of the deprojection in this region. The true x_1-orbits could easily be somewhat less cuspy near their ends, or the x_2-orbits less converging, making them more easily populated with gas clouds.

Thirdly, the hydrodynamic flow in the central MW could be genuinely slower than suggested by the closed orbits that it approximately follows. Increasing the model terminal velocities in the bulge region to match the observations would then require a somewhat larger bulge mass-to-light ratio than the value determined from the TVC fit at $10° < |l| < 50°$. This might be plausible if the disc population is somewhat younger than that of the bulge. It is unlikely that the M/L ratio is significantly larger in the entire central kpc of the MW because the peak velocity of gas on x_2-orbits in our standard gas model is 85 km s^{-1}, which compares well to the observed $\lesssim$ 80 km s^{-1} for CS-cloud cores at $|l| \lesssim 0.7°$, where the projected model x_2-orbits are located. However, the potential near $R \approx 1$ kpc, which is most relevant for the x_1-orbits, is more sensitive to the upper bulge component than that in the inner 100 pc where the x_2-orbits are. The required variations of the bulge M/L to give terminal velocities of $\gtrsim$ 250 km s^{-1} would seem consistent with the spread of K-band mass-to-light ratios for other bulges, e.g. from NIR surface brightness photometry of early-type spirals, Moriondo, Giovanardi & Hunt (1998) obtain a mean value and dispersion (0.6 ± 0.2) $(\mathrm{M}_\odot/\mathrm{L}_\odot)_K$ [the velocity scale of the standard gas model corresponds to $(M/L)_K \approx 0.6$ $(\mathrm{M}_\odot/\mathrm{L}_\odot)_K$].

In summary, there are uncertainties in modelling the gas velocities in the inner few hundred parsecs of the bulge. We will not pursue this further here, because as already discussed in the previous subsection, this is not important for the gas flow in the main spiral arms further out. Rather, we now turn to the determination of the pattern speeds in the Milky Way.

4 THE GAS FLOW IN MODELS WITH SEPARATE BAR AND SPIRAL ARM PATTERN SPEEDS

Fig. 12 shows a time sequence for the gas distribution in our point-symmetric standard model with pattern speeds $\Omega_\mathrm{p} = 60$, $\Omega_\mathrm{sp} = 20$ Gyr^{-1}. The inner arms emanating from the ends of the bar corotate with the bar pattern speed; they are clearly driven by the bar. These inner arms are connected to the outer spiral arms by a time-dependent transition region near bar corotation. Here a lateral arm

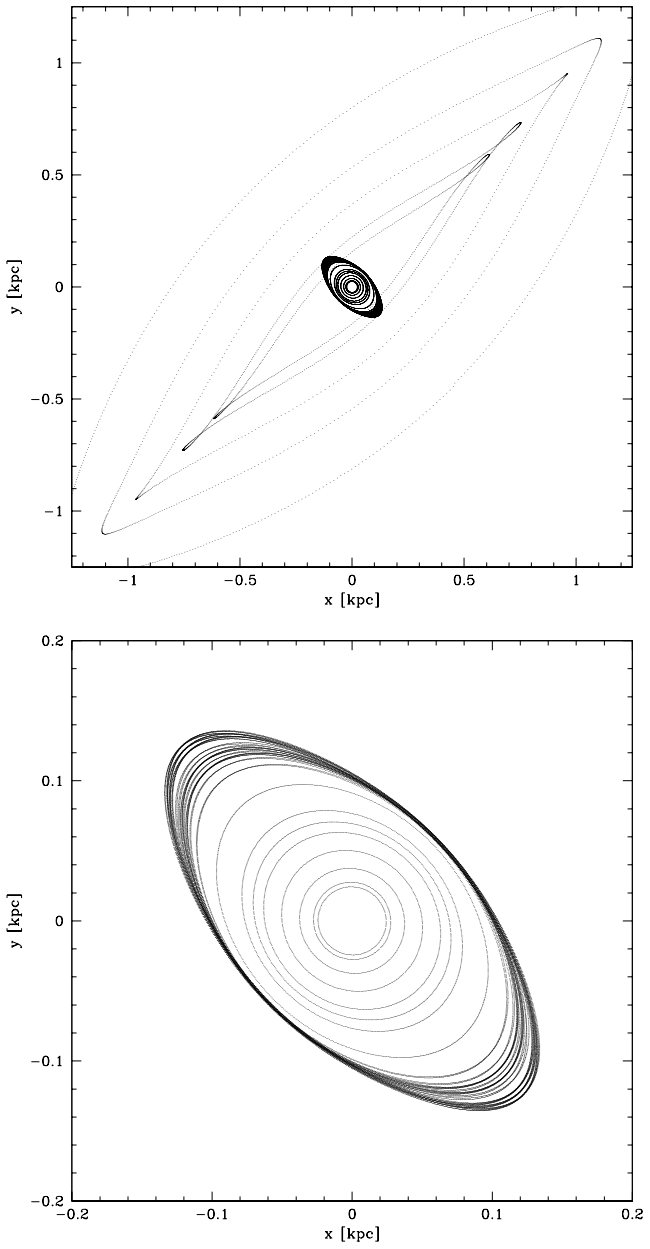

Figure 10. A sample of closed x_1- and x_2-orbits in the bar frame, in the $\varphi_{\rm bar} = 20^\circ$ potential of our standard gas model with pattern speeds $\Omega_{\rm p} = 60$, $\Omega_{\rm sp} = 20$ Gyr^{-1}. Note the convergence of the outer x_2-orbits on the major axis of the bar.

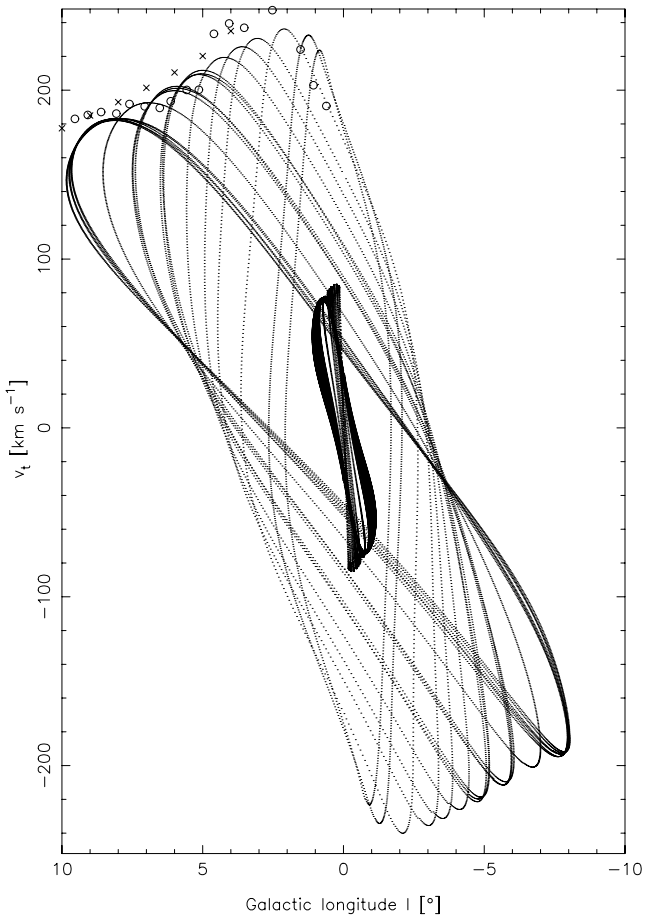

Figure 11. The same orbits as shown in Fig. 10, now displayed in an (l, v) diagram, using $\varphi_{\rm bar} = 20^\circ$ also for the projection. The orbit with the highest peak velocity, at $l \simeq 2^\circ$, is the cusped orbit. Inside this cusped orbit two x_1-orbits with self-intersecting loops are plotted (cf. Fig. 10). Slight oscillations in the (l, v) traces of the outer x_1-orbits betray the time dependence of the potential. All orbit velocities are scaled by the same factor ξ as in the TVC of the standard model in Fig. 6. Also shown in the figure are the observed terminal velocities in the bulge region. The cusped orbit and the other x_1-orbits at larger galactocentric radius represent the observed terminal velocities well. The velocities of x_2-orbits peak at $|v| \simeq 85$ km s^{-1} in the plot.

from the distant end of the bar as seen from the Sun merges with the other inner arm from the nearer end in some frames (4–5), but not in others (1–2). In the latter case, the lateral arm continues into the outer spiral arm passing close to the Sun, in the former both arms join into a weaker outer arm staying well inside the Sun. The outer arms themselves move with respect to the bar frame. However, they do not rotate in the plot steadily around the centre of the model, as one might have expected if they were driven by the different pattern speed of the spiral arm *potential*, but apparently exhibit complicated back-and-forth oscillations, with respect to each other and with respect to the bar frame and some arms merge and bifurcate at certain times; compare the vicinity of $(x, y) = (-5, -3)$ in the different panels.

The outer spiral structure evolves in such a complicated way because both the spiral arm potential and the bar simultaneously force the gas distribution with different pattern speeds. To investigate this further, we have computed a gas model similar to the standard model, but with spiral structure removed from the gravitational potential, so that the non-axisymmetric component of the potential is solely caused by the bar. The resulting model has four spiral arms inside the bar corotation radius and two symmetric outer spiral arms, all stationary in the bar frame. In the model with a driving spiral structure potential, the four outer arms can be regarded as a superposition of one component generated by the bar perturbation, which is at nearly constant position in the bar frame and a second component driven by the spiral structure potential perturbation. The former is the stronger pair of arms in Fig. 12, one of which passes just inside the Sun symbol in the figure. The second component, visible as the weaker pair of arms between the bar-driven arms in Fig. 12, can be seen to fall behind the bar-driven arms through the sequence of frames in Fig. 12 ($\Omega_{\rm p} \gtrsim \Omega_{\rm sp}$). At certain times the second component

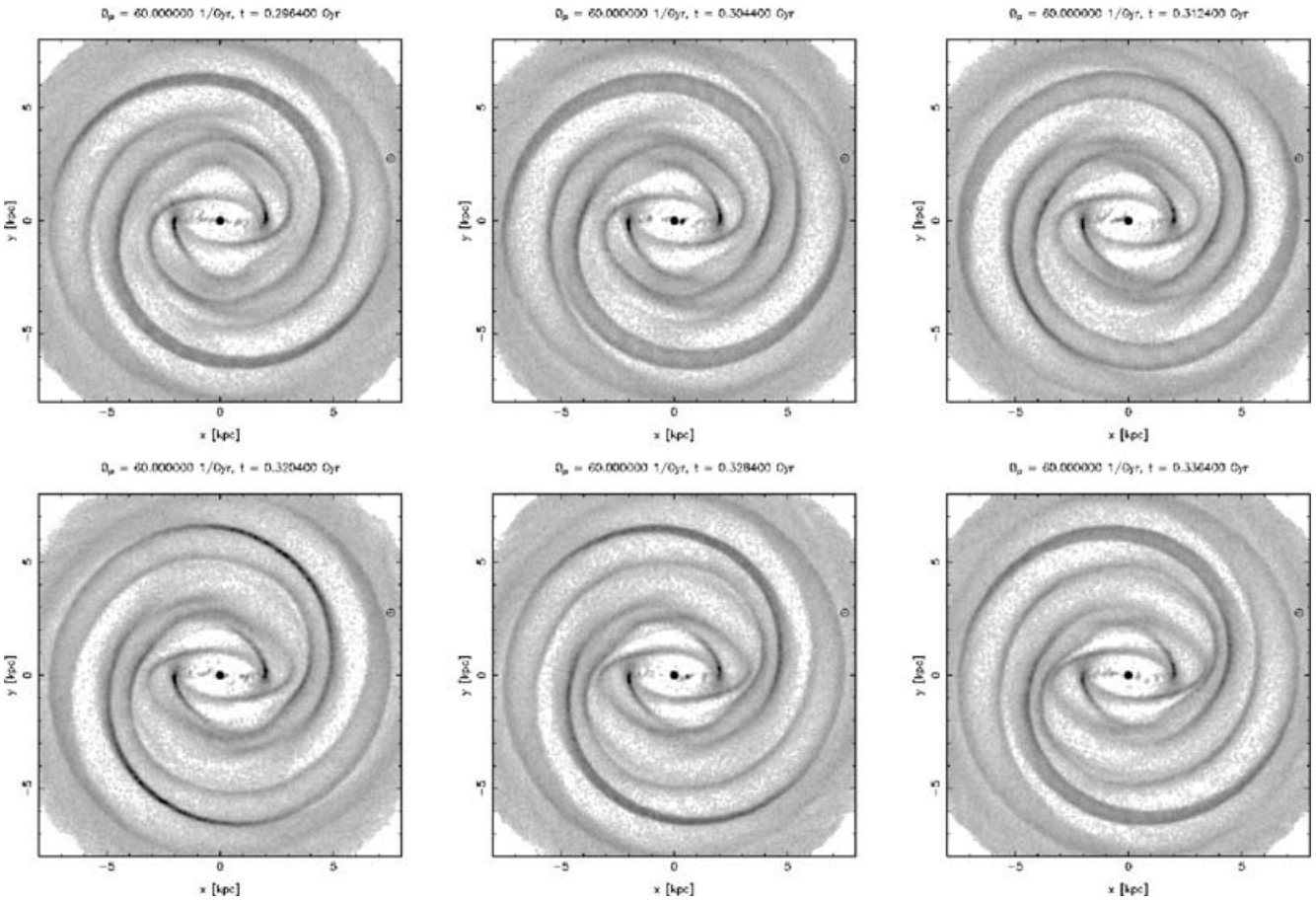

Figure 12. The gas distribution of the standard model 20 for a sequence of evolutionary times and corresponding phase differences between the bar and spiral components of the potential: (0.296 Gyr, 318°), (0.304 Gyr, 337°), (0.312 Gyr, 356°) (upper row from left to right) and (0.320 Gyr, 14°), (0.328 Gyr, 33°) and (0.336 Gyr, 51°) (lower row from left to right). The long axis of the bar is aligned with the *x*-axis in all panels. Note the evolution in the connecting region between the inner and outer arms.

is seen to branch off the bar-driven arms (frame 1). Thereafter, the spiral-driven arm appears to fall behind, move inwards, until it finally collides with the opposite bar-driven arm (frames 2–6 $\simeq$ frames 1–3). In the course of this evolution, the detailed morphology of the transition region around bar corotation changes. At most times, the spiral-driven arms are connected to the inner lateral arms (frames 2–5), at others the latter connect to the bar-driven arms (frame 1). At certain times, an arm may look fragmented and its tangent point may split in longitude.

Thus when neither the bar nor the spiral structure component dominates the non-axisymmetric potential and gas flow in the disc, as in Fig. 12, it is difficult to deduce from a single snapshot of the arm morphology that the system supports a second, independent pattern speed. This may explain why it is difficult to say from the observed arm morphologies in barred spiral galaxies whether the spiral arms are driven by the bar or not (see Sellwood & Wilkinson 1993).

4.1 Pattern speeds in the Milky Way

We now investigate Galactic models with different combinations of the bar pattern speed $\Omega_{\rm p}$ and the spiral arm pattern speed $\Omega_{\rm sp}$. Particularly for the spiral arms the assumption of a constant pattern speed is probably still idealized, but represents a first step towards understanding realistic cases. In these models, the separation of bar and spiral arm components in the potential is based on the density distribution. We assume that the $m \geqslant 2$ multipoles of the density at galactocentric radii $r < r_{\rm cut} = 3.5$ kpc (bar) rotate with $\Omega_{\rm p}$, and outside of $r_{\rm cut}$ (spirals) with $\Omega_{\rm sp}$. The specific value of $r_{\rm cut}$ was chosen because it corresponds approximately to the end of the bar in the reference luminosity model of Paper II and is also equal to the inner radius of the spiral pattern there. All models described in this section are based on this luminosity model (cf. Section 2.1).

Multiple pattern speeds ($\Omega_{\rm p} \neq \Omega_{\rm sp}$) imply a genuinely time-dependent potential in the frame corotating with the bar. For each model we have therefore investigated a sequence of snapshots at different evolutionary ages, separated by $\Delta\phi \approx 23^\circ$ in phase difference between the two components in the potential. This corresponds to steps in the evolutionary age of the model of ≈0.01–0.02 Gyr, depending on the combination of pattern speeds. A finer analysis of our standard gas model in steps of $\Delta\phi \approx 9^\circ$ showed that no significant features in the models are missed with $\Delta\phi \approx 23^\circ$. Because the potentials used in this section are point-symmetric, we need to cover only a range of 180° in bar–spiral phase difference. All analysed snapshots have evolutionary ages at or around 0.30 Gyr, the time after which the gas flow in the similar single-pattern speed models of Paper I had become approximately quasi-stationary.

We begin with the three models 60, 40 and 20 with different spiral arm pattern speeds $\Omega_{\rm sp} = 61.4$, 40 and 19.6 Gyr^{-1}. The bar pattern

speed is set to 61.4 Gyr^{-1} (60 Gyr^{-1} for model 20), based on the results of Paper I. Model 60 is the single-pattern speed model; the two other values for $\Omega_{\rm sp}$ are motivated as follows. First, Amaral & Lépine (1997) preferred the lower value $\Omega_{\rm sp} = 20\ \mathrm{Gyr}^{-1}$, based on the positions and ages of open clusters and from comparing their model with other data. Fernández et al. (2001) obtained a somewhat higher $\Omega_{\rm sp} \approx 30\ \mathrm{km\,s}^{-1}\ \mathrm{kpc}^{-1}$ from *Hipparcos* data for OB stars and Cepheids, supplemented with radial velocities or distances, respectively. Thus we selected $\Omega_{\rm sp} = 40\ \mathrm{Gyr}^{-1}$ as an additional intermediate value between $\Omega_{\rm sp} = 20\ \mathrm{Gyr}^{-1}$ and the single-pattern speed model. Secondly, for $\Omega_{\rm sp} = 60$, 20, 40 Gyr^{-1}, the bar corotation radius coincides approximately with the corotation, inner Lindblad and inner ultraharmonic (1:4) resonance of the spiral pattern, respectively (see Fig. 3).

What are the characteristic differences between these models? In Fig. 13 we compare their spatial gas distributions. All three models have four inner spiral arms inside bar corotation (at ≈3.4 kpc) and four outer spiral arms outside of a transition region beyond the end of the bar. Because we have always selected the snapshot of a model that best reproduces the observed (l, v) diagram (Fig. 4), the spiral arm tangent points are fixed relative to the position of the Sun. Thus in the figure the outer arms of all models appear approximately at the same positions.

However, near the bar corotation radius the models differ significantly. In the single-pattern speed model 60, where the spiral structure corotation radius coincides with that of the bar, the gas in the corotation region moves with near-sonic velocities relative to the pattern. Consequently, shocks are weak or non-existent in this region and the spiral arms in the gas response dissolve there. On the other hand, for model 40 with $\Omega_{\rm sp} = 40\ \mathrm{Gyr}^{-1}$, the corotation radius of the spiral structure is at ≈5 kpc. Again, the gas distribution shows gaps in the spiral arms at this location – one pair of arms nearly vanishes there, the other pair weakens – but there is no such gap in the spiral arms near bar corotation. Rather, the connection between the inner and outer spiral arms is dynamic, owing to the different pattern speeds. Finally, in model 20 the spiral structure corotation radius occurs beyond the solar orbit. In this model we see no clear gaps in the arms. However, near the bar corotation radius $R_{\rm cr}^{\rm bar} \approx$ 3.4 kpc, which coincides with the inner Lindblad resonance of the spiral pattern, the arms weaken and the transition region appears to be more complicated than in model 40.

The comparison with the Galactic TVC is shown in Fig. 14. All three models reproduce the observed data quite well, but the slope in the region $10^\circ \leqslant |l| \leqslant 50^\circ$ is fitted significantly better by the multiple pattern speed models than by the single-pattern speed model. For $|l| \gtrsim 40^\circ$–50° the model TVCs start to fall below the observed TVC; as we have discussed in Section 3, for the assumed $V_0 = 220$ km s^{-1} the dark halo starts to contribute to the observed velocities there, according to our NIR-based models.

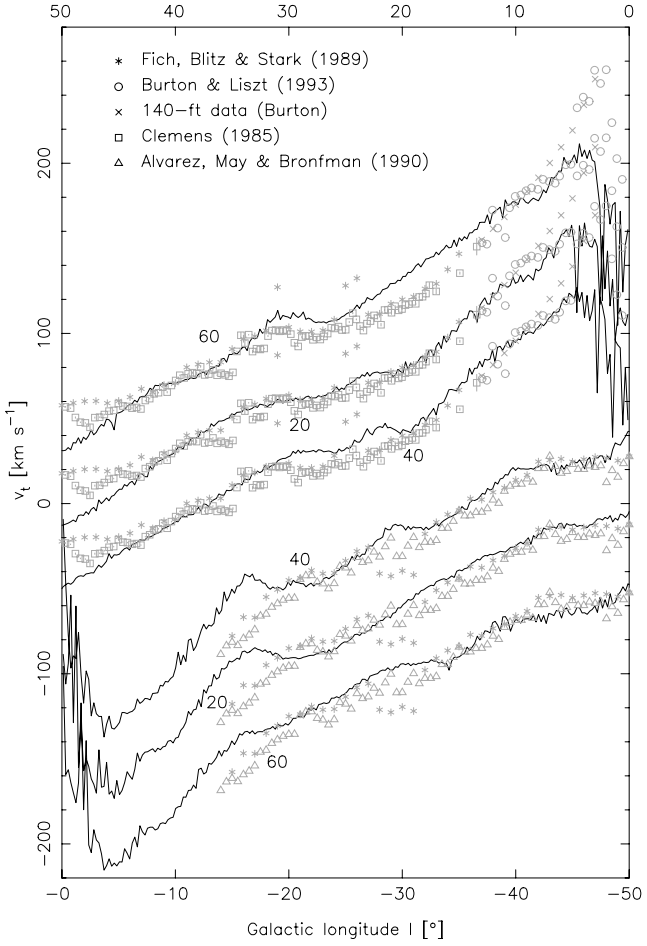

Figure 14. Terminal velocity curves for the best evolutionary ages of the single and double pattern speed models 60, 20 and 40. The model TVCs are scaled by different factors ξ, determined, respectively, from the best fit to the observations for $10^\circ \leqslant |l| \leqslant 50^\circ$. For clarity, the TVCs are separated by 40 km s^{-1} from each other in velocity.

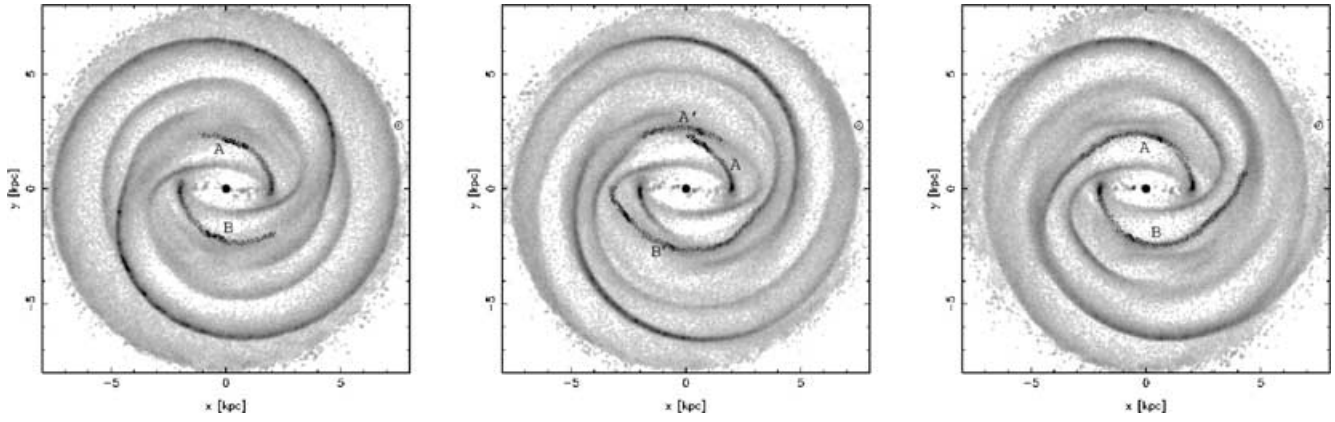

Figure 13. Gas distribution in models 60 (left), 20 (middle) and 40 (right). Overplotted black dots indicate particles highlighted in the (l, v) diagrams in Fig. 15. The position of the Sun at (x, y) ≈ (7.5 kpc, 2.7 kpc) is shown by the ⊙ symbol.

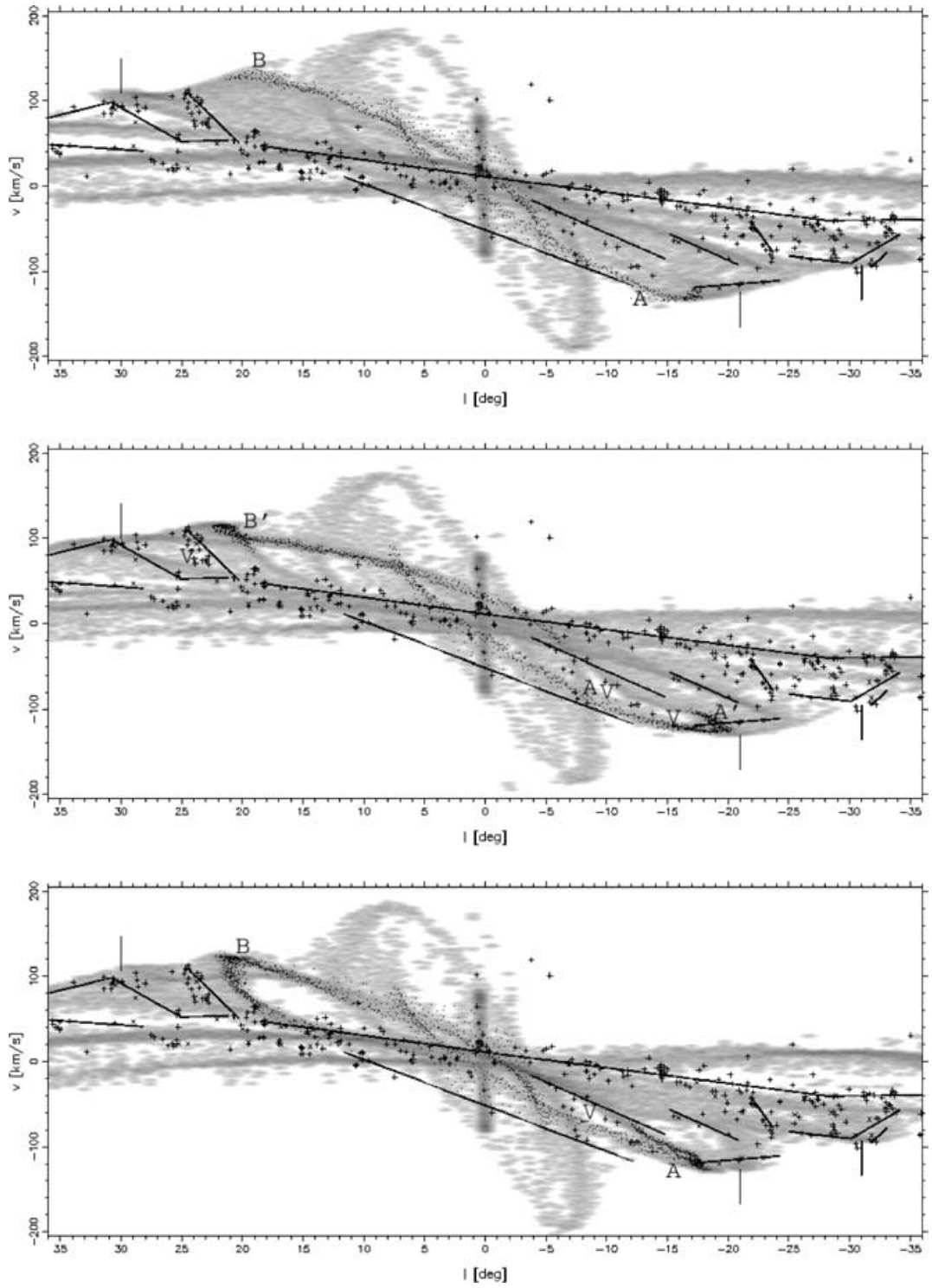

Figure 15. (l, v) diagrams for the best evolutionary times of models 60 (at age 0.30 Gyr, top), 20 (at 0.32 Gyr, middle) and 40 (also at 0.32 Gyr, bottom). The model velocities are scaled by the same factor ξ as the respective TVC in Fig. 14; the LSR velocity is 220 km s^{-1}. Particles in low surface density regions are suppressed to enhance the contrast as described in the caption of Fig. 8. For comparison with observations, spiral arm ridge lines from Fig. 4, positions of giant molecular clouds ('$\times$' symbols) and H II regions ('+' symbols) from Fig. 8, and spiral arm tangent directions from Englmaier & Gerhard (1999) are overplotted.

Fig. 15 shows (l, v) diagrams for the three models. To facilitate their interpretation, we have overplotted a number of observed features and have highlighted particles belonging to specific arm features both in this figure and in the density plots of Fig. 13, labelled by 'A' and 'B'. Feature 'A' corresponds to the 3-kpc arm in the observed CO (l, v) diagram (Fig. 4), feature 'B' to its symmetric counter-arm in the models (see Fig. 13; in model 20 the neighbouring arm 'A' is included).

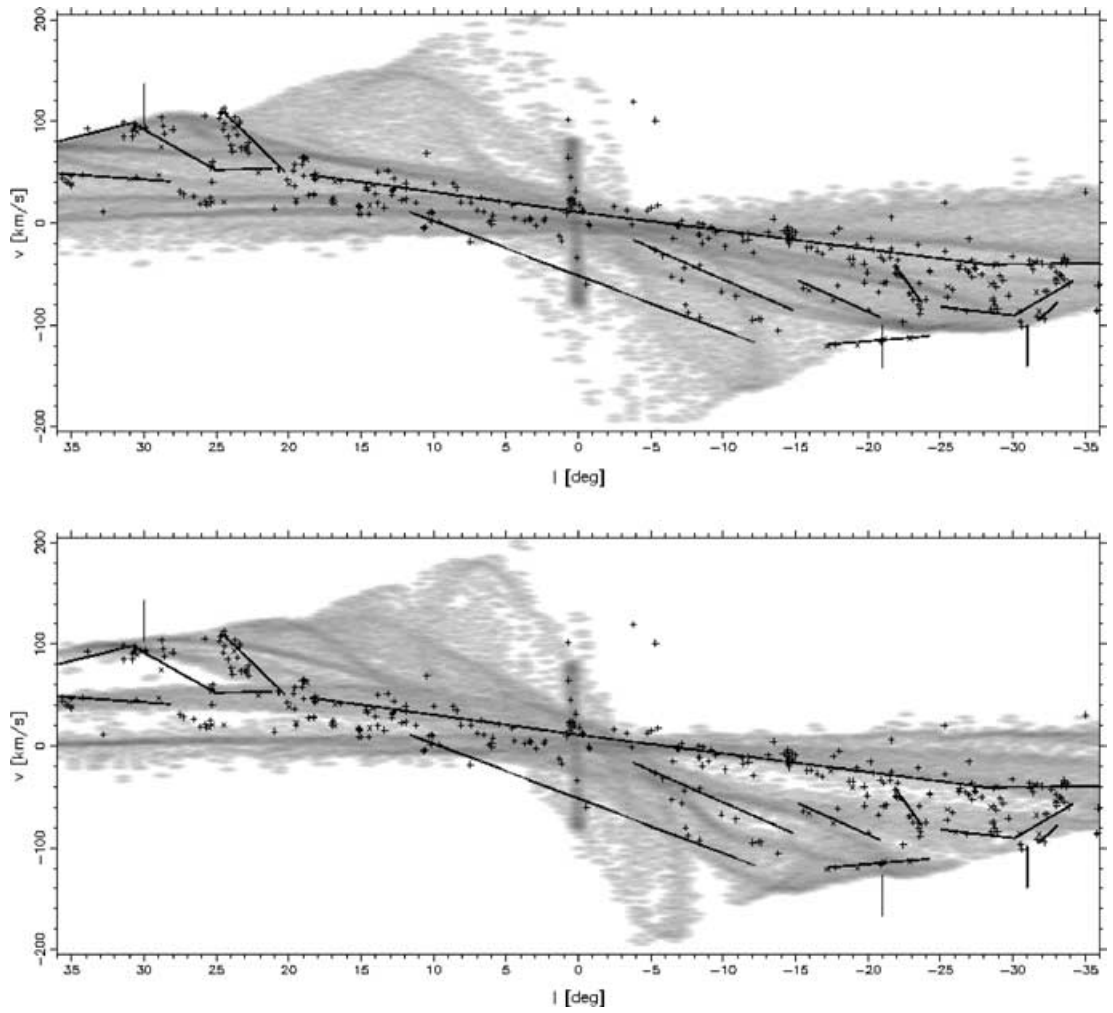

Figure 16. (l, v) diagrams for the best evolutionary time 0.307 Gyr of model bar50 (top, $\Omega_p = 50$ Gyr^{-1}) and for 0.321 Gyr of model bar70 (bottom, $\Omega_p = 70$ Gyr^{-1}), with model velocities scaled as described in the caption of Fig. 6. Overplotted data are the same as in Figs 8 and 15.

Particularly important is the existence of certain regions in the (l, v) diagram, e.g. next to the 3-kpc arm (feature 'A'), where hardly any gas is found in the multiple pattern speed models. Such voids, designated by 'V' in the plots, arise because the gas is aligned morphologically and kinematically with spiral arms there, which appear as well-defined ridges with adjacent voids in the (l, v) diagram. From Fig. 4 we see that similar voids are also visible in the observed ^{12}CO (l, v) diagram, specifically next to features 'A' and 'B' in the bar corotation region. This suggests strongly that in the MW the gaseous arms go through bar corotation. In contrast, in the single-pattern speed model 60, the arms dissolve in the bar corotation region, the 3-kpc arm is thus incomplete and the gas is spread out approximately evenly over the corresponding parts of the (l, v) diagram. Models with a separate second pattern speed for the spiral arms in the MW are therefore preferred over single-pattern speed models. Models with a growing bar amplitude also support spiral arms in the corotation region (Thielheim & Wolff 1982); however, it is probable that when self-gravity is included and the amplitude becomes non-linear, the growing spiral pattern will again develop an independent pattern speed.

Overall, the models in Fig. 13 provide a good match to the observed CO (l, v) diagram. The main features that are reasonably well represented are: the arm tangent at $l = 30^\circ$; the observed $l = 25^\circ$ tangent, although at smaller $l \simeq 20^\circ$ in models 20 and 40; the morphology of this arm; the location of the main spiral arm leading to the $l = 50^\circ$ tangent; the morphology of the ridges and voids at $-10^\circ > l > -25^\circ$ (apart from model 60); the arm morphology around $(l, v) = (20^\circ, 60$ km s$^{-1})$. The main weaknesses of the models, if we disregard the poorly resolved bulge region, are: the arm in the models, which returning from the $l = 20^\circ$ tangent, crosses the region $5^\circ \lesssim l \lesssim 10^\circ$ at $v > 50$ km s^{-1} and does not have a counterpart in the data, except perhaps if shifted to lower velocities; the missing tangent at $l = -30^\circ$ in models 60 and 20; the displacement of the 3-kpc arm towards lower velocities.

In model 20, the spiral arm corresponding to the Centaurus tangent at $l \approx -51^\circ$ is strongest when one of the spiral-driven arms coincides with the bar-driven arm (e.g. frames 3 and 4 in Fig. 12). Shortly before and after this evolutionary time this arm looks fragmented in the model and its tangent point appears split in longitude. Indeed, there are observational indications that the Centaurus tangent is split into two parts at $l \approx -50^\circ$ and $\approx -55^\circ$ (to 58°) (cf. table 1 of Paper I).

The displacement of the 3-kpc arm in the model and the apparent absence of its counter-arm in the data might indicate a non-point-symmetric mass distribution in this region. This possibility is discussed further in Section 5.4. Also, in models where the

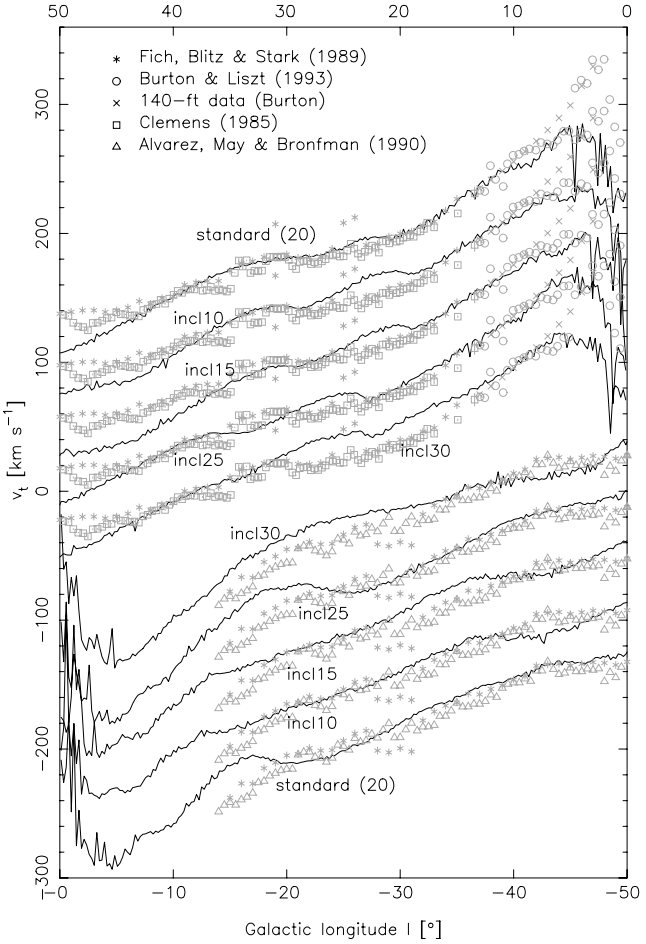

Figure 17. TVCs at the respective best evolutionary time, for a sequence of models with bar angles $\varphi_{\rm bar} = 10^\circ$ (model incl10, at age 0.32 Gyr), $\varphi_{\rm bar} = 15^\circ$ (model incl15, at age 0.32 Gyr), $\varphi_{\rm bar} = 25^\circ$ (model incl25, at age 0.31 Gyr) and $\varphi_{\rm bar} = 30^\circ$ (model incl30, at age 0.30 Gyr). For comparison, the standard model 20 for bar angle $\varphi_{\rm bar} = 20^\circ$ is included in the figure. In all models the pattern speeds are $\Omega_{\rm p} = 60$ Gyr^{-1} and $\Omega_{\rm sp} = 20$ Gyr^{-1} and model velocities have been scaled by factors ξ, determined for each model by fitting the observed terminal velocities for $10^\circ \leqslant |l| \leqslant 50^\circ$. For clarity, these TVCs have been offset in steps of 40 km s^{-1}, with model incl15 plotted at the correct velocities.

spiral pattern speed differs from the bar pattern speed, we also expect the *mass distribution* in the transition region to be generally time-dependent. Thus in this region the mass distribution based on the NIR data can represent only one snapshot in time. In addition, there is not much information in the NIR data on the spiral arm heads in this crucial transition region, to constrain the luminosity model of Paper II. Hence the potential in this region is likely to be at best approximately correct.

In summary, the multiple pattern speed models reproduce the observed features in the bar corotation region better than the single-pattern speed model, in particular the regions void of gas in the (l, v) diagram near the 3-kpc arm. Comparing the lv-plots for models 20 and 40, we have found a slight preference for model 20 from the positions of the spiral arms; however, the differences between these two models are too small to determine the spiral arm pattern speed reliably. We take the model with $\Omega_{\rm sp} \simeq 20$ Gyr^{-1} as our standard model, and use this pattern speed in the following.

We now proceed to determine the best bar pattern speed $\Omega_{\rm p}$. To this end we consider two models bar50 and bar70 which have $\Omega_{\rm p} = 50$ Gyr^{-1} and 70 Gyr^{-1}, respectively. For both models, we set $\Omega_{\rm sp} = 20$ Gyr^{-1}; since the differences between models 20 and 40 are small, the precise choice of $\Omega_{\rm sp}$ should not matter. Fig. 16 shows (l, v) diagrams for the respective best evolutionary times of models bar50 and bar70. For both models the fit of the spiral ridges in the inner disc region of the (l, v) diagram is significantly worse than for the models with $\Omega_{\rm p} \approx 60$ Gyr^{-1}. In model bar50 the positions of the spiral arm ridges and tangents are worse (e.g. one of the $l > 0$ tangents is missing) and the $l < 0$ TVC and the 3-kpc arm are particularly poorly represented. In model bar70 the spiral arm ridge with tangent position at $l \approx 25^\circ$ is at significantly too small longitudes and the same is true for the Centaurus tangent near $l \approx -51^\circ$, which corresponds to one of the bar-driven outer arms (see the discussion above). It is noteworthy that the position and shape of the Centaurus tangent are sensitive to $\Omega_{\rm p}$ despite a galactocentric radius of this tangent point of more than 6 kpc. Note also that a pattern speed of 70 Gyr^{-1} would put corotation inside the end of the NIR bar (see Section 2 and Paper II).

We conclude that the best value for the bar pattern speed in the Milky Way is $\Omega_{\rm p} = (60 \pm 5)$ Gyr^{-1}. For the preferred scaling of the employed NIR bar model this corresponds to bar corotation at 3.4 ± 0.3 kpc, equal to the length of the bar within the uncertainties. I.e. the Milky Way bar is a fast bar.

5 BAR ORIENTATION AND INFLUENCE OF STELLAR SPIRAL ARMS

5.1 Bar angle

In Paper II, luminosity models were generated from the *COBE*/DIRBE L-band data for bar angles $\varphi_{\rm bar} = 10^\circ$, 15°, 20°, 25°, 30° and 44° in the same way as for the standard $\varphi_{\rm bar} = 20^\circ$ model. From considering the photometric residuals and the line-of-sight distributions of clump giant stars in the bulge, a preferred range for the bar angle $15^\circ \leqslant \varphi_{\rm bar} \leqslant 30^\circ$ was found. Here we obtain independent constraints on $\varphi_{\rm bar}$ from corresponding gas flow models.

For each value of the bar angle, the luminosity model was converted to a mass model assuming constant M/L. As described above, the non-axisymmetric part of the potential was split into bar and spiral arm components and gas models were computed with pattern speeds $\Omega_{\rm p} = 60$ and $\Omega_{\rm sp} = 20$ Gyr^{-1}, respectively. In Figs 17 and 18 we show the TVCs and (l, v) diagrams of models incl10, incl15, incl25 and incl30 with bar angles $\varphi_{\rm bar} = 10^\circ$, 15°, 25°, 30° at their respective best evolutionary times, as judged by comparing their (l, v) diagrams with Fig. 4.

Model incl25 reproduces the terminal velocity observations with similar quality as the standard gas model 20, but model incl30 is clearly inferior – the terminal velocities are too large at positive longitudes and too small in modulus at negative longitudes. Obviously, this cannot be corrected for by a change of the velocity scaling factor ξ. The TVCs of models incl10 and incl15 are also inferior fits to the observed terminal velocities, albeit not as bad as model incl30.

The (l, v) diagrams of these models depend strongly on the assumed bar angle. Models incl10, incl15 and incl30 do not reproduce the observed spiral arm ridges. Models incl10 and incl15 also do not have a well-defined 3-kpc arm at positive longitudes and model incl30 shows very little arm structure at all in the region around bar corotation. Model incl25 reproduces the observations

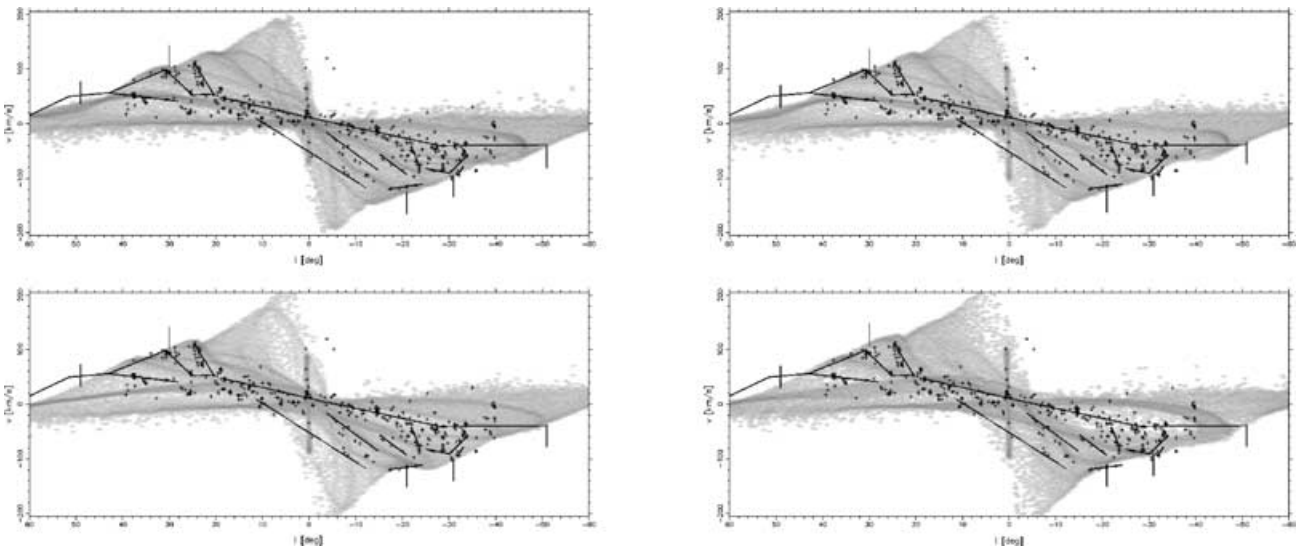

Figure 18. (l, v) diagrams for the gas flow models with bar angles 10° (top left), 15° (top right), 25° (bottom left) and 30° (bottom right), for the same evolutionary times as in Fig. 17.

for a large range of longitudes nearly as well as the standard model, but the positions of the spiral arm ridges at $-30^\circ \lesssim l \lesssim -10^\circ$ are not matched well and the non-circular velocities in the 3-kpc arm are smaller than in the standard $\varphi_{\rm bar} = 20^\circ$ model. From the (l, v) diagrams model 20 is best, but we consider model 25 as still satisfactory.

One may ask, how much of the difference between these models is as a result of the different shapes of their underlying luminosity distributions and gravitational potentials and how much of it is due simply to the different viewing geometries with respect to the gas flow? To answer this question, we have constructed the (l, v) diagram of the standard gas model 20 seen from a viewing angle of $\varphi_{\rm bar} = 30^\circ$. The morphology of the arms in this (l, v) diagram differs little from that in the original $\varphi_{\rm bar} = 20^\circ$ (l, v) diagram because of the tightly wound pattern. Thus the differences between the (l, v) diagrams in Fig. 18 must be caused mainly by genuine changes in the gas flow, originating from the different mass distributions corresponding to the *COBE* data for different $\varphi_{\rm bar}$.

5.2 Spiral arm models

The MW very probably has four spiral arms in the gas distribution (e.g. Englmaier & Gerhard 1999). It is not clear, however, whether these also correspond to four *stellar* spiral arms, because some of the tangent points are not clearly seen in the near-IR light (see the discussion in the introduction and in Drimmel & Spergel 2001). Here we investigate the (l, v) diagrams that result when different stellar spiral arm patterns drive the gas flow and also findevidence for a four-armed spiral pattern in the distribution of luminous mass. Specifically, we have studied three models.

Open2. A two-armed model with the same spiral arm pitch angle 13.8° as in the standard (four-armed) mass model, but where the Sag-Car arm and its counter-arm are removed from the model. Such a model can be justified by the fact that the Sag-Car arm is hardly visible in the NIR.

2spi. Another two-armed model, but with approximately half the pitch angle of the standard four-armed model. This model reproduces approximately the same tangent point positions on the sky as the standard model.

Mix. Similar to the standard mass model, but the Sag-Car arm and its counter-arm are given only 40 per cent of the peak density amplitude of the other two arms. This is based on the result of Drimmel & Spergel (2001), who found that they had to reduce the amplitude of the Sag-Car arm in their best-fitting four-armed model for the *COBE*/DIRBE *J*- and *K*-band NIR maps.

Luminous mass models with these patterns were derived using the algorithm described in Paper II, all for bar angle $\varphi_{\rm bar} = 20^\circ$, by incorporating the respective spiral arm model in both the parametric initial model and in a penalty term for the non-parametric deprojection. As in the standard mass model the non-parametric algorithm changes the spiral arms somewhat, but the overall pattern stays intact. Because the NIR data constrain only the arm tangent points (Paper II), two- and four-armed models that reproduce the tangent point data fit the photometry with similar quality.

The TVCs of gas flow models computed in the corresponding gravitational potentials are shown in Fig. 19. The overall slope with l of all of these model TVCs is similar, because this is dominated by the monopole term in the mass distribution. However, all three models open2, 2spi and mix do not fit the wavy structure of the TVC data and the standard model 20 (Fig. 6), with model mix being the best among the three. For comparison we also include in Fig. 19 the TVC of a model noarms, the gas flow of which was determined in a potential that includes only the perturbation from the bar, but not that from the spiral arms. This model has only two outer spiral arms in the gas distribution.

(l, v) diagrams of these models are shown in Fig. 20. Models open2 and 2spi compare poorly with the observed CO (l, v) diagram: the up-turning arm at $l \approx 25^\circ$ is missing and the spiral structure is generally wrong for $-15^\circ \lesssim l \lesssim -35^\circ$. In both these models the fit to the data is poor because the gas distribution of the model is only two-armed. We have checked that this is not a result of choosing the wrong bar and spiral arm pattern speeds, by computing gas models in the two-armed potential of model open2 for the additional combinations of ($\Omega_{\rm p} = 50$ Gyr^{-1}, $\Omega_{\rm sp} = 20$ Gyr^{-1}) and $\Omega_{\rm p} = \Omega_{\rm sp} = 60$ Gyr^{-1} (single-pattern speed). In both cases, the global, two-armed morphology of the gas flow is the same as in model open2. Model mix is the best of the three models in this section. However, the envelope of its lv-plot shows stronger bumps than the standard

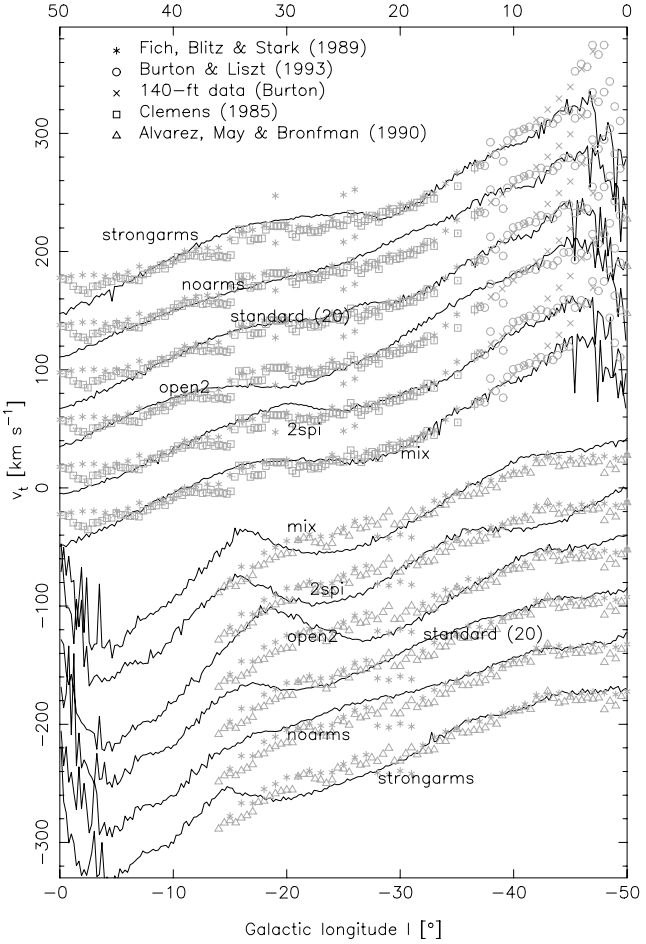

Figure 19. TVCs at the respective best evolutionary time, for gas models forced by different types of spiral structure in the mass density. Model open2 is shown at age 0.30 Gyr, model 2spi at age 0.30 Gyr and model mix at age 0.31 Gyr, model strongarms at age 0.32 Gyr. Also shown is the standard model 20 and model noarms without any massive spiral arms. For all models, the pattern speeds are $\Omega_p = 60$ Gyr^{-1} and $\Omega_{sp} = 20$ Gyr^{-1}, and the velocity scale is fixed by fitting to the observed terminal velocities for $10^\circ \leqslant |l| \leqslant 50^\circ$. For clarity, the model TVCs are offset in steps of 40 km s^{-1}, with model open2 plotted at the correct velocities.

model, in particular near $-30^\circ, \ldots, -15^\circ$. The gravitational potential of model mix is quite similar to our standard potential and therefore the similarity of the gas flows is expected. From these tests we conclude that a four-armed spiral arm potential is preferred (see also Englmaier & Gerhard 1999; Fux 1999).

5.3 Stronger spiral arms

The standard gas model fits most spiral arms in the observations well. However, the famous 3-kpc arm, a prominent feature that extends from ($l \approx 10^\circ$, $v = 0$ km s^{-1}), through ($l = 0^\circ$, $v \approx -50$ km s^{-1}), to ($l \approx -22^\circ$, $v \approx -120$ km s^{-1}) is still displaced towards lower non-circular velocities. Because the underlying mass model already contains spiral arms, assigning gravitating mass to the gas particles does not lead to an improvement (as a corresponding model confirmed).

However, compared with near-IR observations of other spiral galaxies (cf. Rix & Zaritsky 1995), our standard mass model has rather narrow and weak spiral arms. This might be simply because only the positions of the spiral arm tangents are constrained by the *COBE*/DIRBE *L*-band data, while the spiral arm heads near the bar are not well-constrained. It is therefore possible that our standard mass model underestimates the strength of the Galactic spiral arms. We have therefore investigated a model strongarms in which we enlarged non-axisymmetric forces in the disc, by multiplying with 1.5 the $m \geqslant 2$ multipoles of the spiral arm component (i.e. the component corresponding to the density outside of $r_{cut} = 3.5$ kpc) in the standard model and computed the gas flow in this modified potential.

We show in Fig. 19 the TVC and in Fig. 21 the (l, v) diagram of this model strongarms. The fit to the TVC observations is not as good as for the standard model 20, but in the (l, v) diagram the spiral arm ridges are quite similar. Owing to the stronger spiral arm gravity, the bumps in the terminal velocity are somewhat stronger, but still in the acceptable range. Interestingly, the 3-kpc arm now fits the observations nearly perfectly. This shows that the strength of the spiral arms is an important parameter for the observed kinematics of the 3-kpc arm and the non-circular motions in this region of the Galactic (l, v) diagram cannot simply be used to determine the bar aspect angle (cf. Weiner & Sellwood 1999). It also suggests that our standard model can be improved when a better spiral arm model becomes available.

5.4 Asymmetric models

There are indications in the H I and CO surveys that the gas distribution of the inner Galaxy deviates significantly from point symmetry with respect to the centre. An example is the 3-kpc arm, which has no clear counter-arm in the observed (l, v) diagrams. That is not to say that there is no counter-arm; if asymmetric, its inner parts could, for example, appear at similar locations in Fig. 4 as the arm that reaches the TVC at $l \approx 25^\circ$. All symmetric mass models, however, yield counter-arms with approximately the same absolute velocities as the 3-kpc arm. A way out of this dilemma has been shown by Fux (1999). In his model, the 3-kpc arm and its counter-arm are significantly disturbed by strong non-axisymmetric modes in the Galactic Centre, and in the outer disc. Such a mechanism may also help to explain that the peak in the terminal velocity at $l = +2^\circ$ appears to be much higher than at $l = -2^\circ$ in the CO data. In addition, the x_2-disc in the centre may be disturbed by this effect and this might explain the uneven gas distribution seen in CS. There is no evidence for an asymmetric mass distribution in the NIR data, so in our mass models we can only introduce asymmetry in the density by hand and study the consequences.

To this end, we first created uneven m modes in the disc by weakening one or two arms in the initial model, or by moving two spiral arms closer together. In such gas models we observed strong effects on the position of gas shocks and their relative strength in the outer disc. Some cases look similar to the result of Fux with an almost three-armed outer disc structure. However, the inner arms, especially the 3-kpc arm, did not change much. Only in an extreme case have we been able to move the 3-kpc arm to higher velocities, while simultaneously the counter-arm was moved to lower velocities, but this model does not fit the observations well overall.

In a second class of asymmetric models, we let the stellar bar centre rotate on a circular orbit with radius R_{bar} and pattern speed $\Omega_c = -60$ Gyr$^{-1} = -\Omega_p$, i.e. the centre rotates backwards with respect to the bar and with the same pattern speed as the bar. This also introduces a third parameter, the phase α_{bar} of the bar centre rotation at model age 0.00 Gyr. This approach was motivated by *N*-body

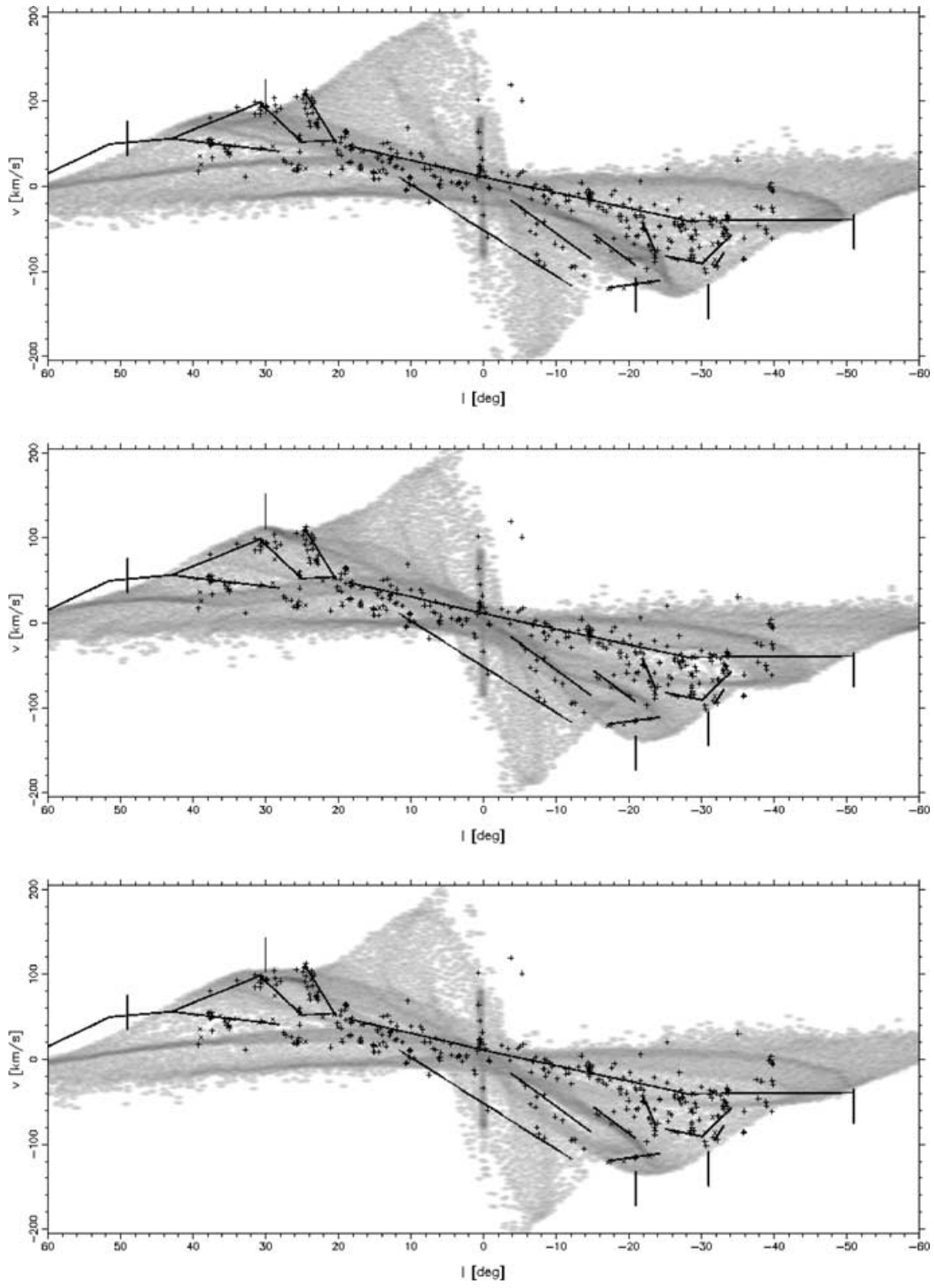

Figure 20. (l, v) diagrams of the models with TVCs shown in Fig. 19, with their respective velocity factors ξ. From top to bottom: model open2, model 2spi and model mix.

simulations (Debattista, in preparation). In simulation tumblingbar ($\Omega_c = -60\,\mathrm{Gyr}^{-1}$, $R_{\mathrm{bar}} = 800$ pc, $\alpha_{\mathrm{bar}} \approx 80^\circ$), we see the 3-kpc arm and its counter-arm move in the right direction in the (l, v) diagram of the model (Fig. 22) and the 3-kpc arm fits the observations well. However, we have not found a snapshot of a model at which the 3-kpc arm, its counter-arm and the overall spiral pattern all fit the data well.

Obviously, the available freedom in introducing deviations from point symmetry is very large. We have only tested a few attractive possibilities and these models show that asymmetries in the Galactic

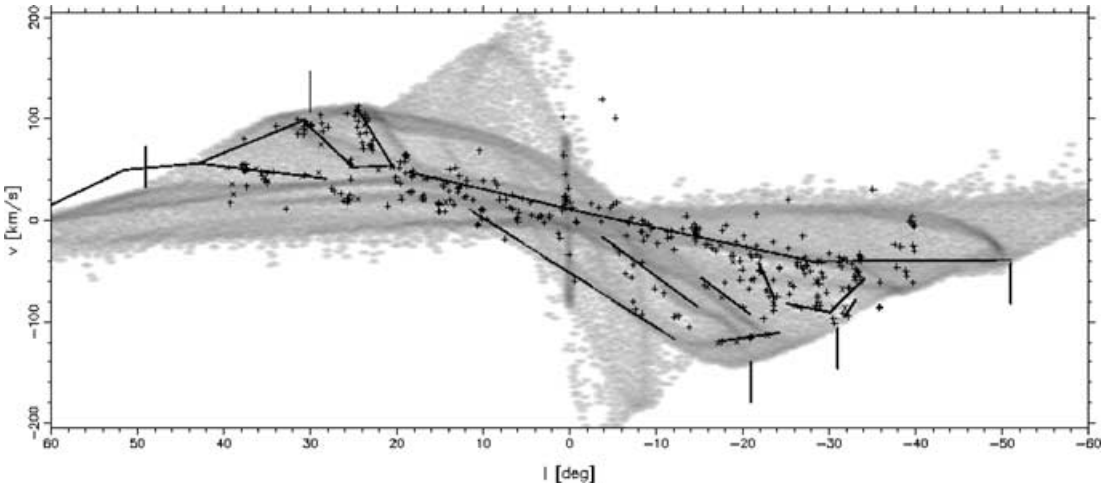

Figure 21. Lv-plot for model strongarms that has strong spiral arms in the potential, at its best evolutionary age 0.32 Gyr. Model velocities have been scaled by an appropriate factor ξ, as described in the caption of Fig. 17.

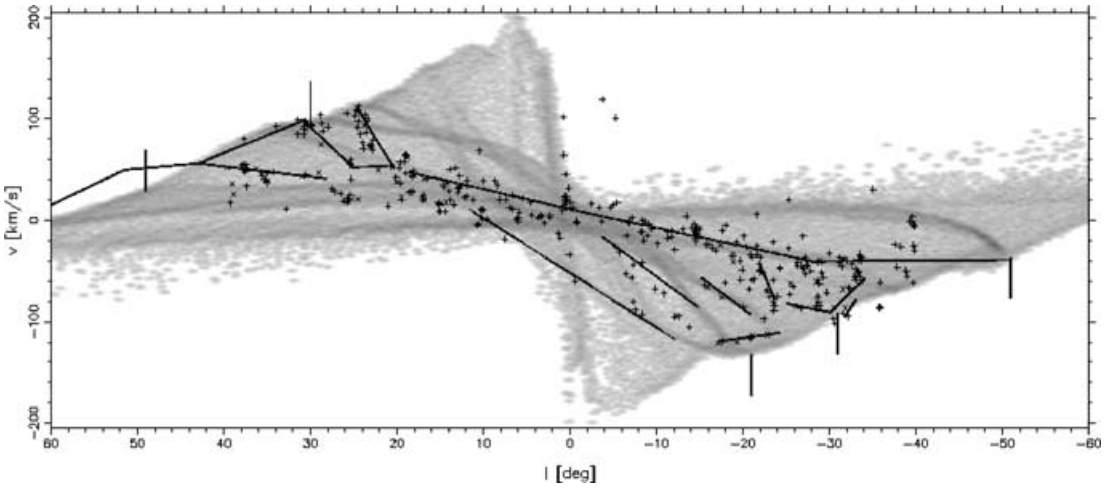

Figure 22. (l, v) diagram for the best evolutionary age (0.32 Gyr) of model tumblingbar. In this model the centre of the stellar bar is offset from the galaxy centre by 300 pc, and rotates around it with $-\Omega_p$. Note that the 3-kpc arm is reproduced well, but not its counter-arm.

mass distribution may be important and could be at the root of some of the remaining problems in our standard model.

6 SUMMARY AND CONCLUSIONS

We have used new gas flow models to investigate the dynamics of the Milky Way Galaxy from observed (l, v) diagrams. Steady-state gas flows in rotating, point-symmetric gravitational potentials for the Galactic bar and disc were determined with SPH simulations. The potentials were derived from non-parametric estimates of the spatial near-infrared luminosity density (Bissantz & Gerhard 2002), based on the dereddened *COBE*/DIRBE *L*-band map of Spergel et al. (1995), but also incorporating clump giant star count data from Stanek et al. (1994, 1997). The luminosity models contain a spiral arm model for the disc and were converted to mass models assuming a constant mass-to-light ratio in the inner MW.

Our best gas flow model gives a very good fit to the Galactic terminal velocity curve for $|l| > 15^\circ$ and to the spiral arm ridges in the observed CO (l, v) diagram. This has enabled us to investigate a number of dynamically important parameters such as the bar and spiral arm pattern speeds, the multiplicity of the spiral structure in the potential and the bar angle. The main results from this study are as follows.

(i) In gas flow models with separate pattern speeds Ω_p for the bulge/bar and Ω_{sp} for the spiral pattern, the spiral arms go through the bar corotation region. Thus (l, v) diagrams of such models show well-defined spiral arm shocks (ridges) through corotation, next to areas that appear to be nearly void of gas. In contrast, in single-pattern speed models the spiral arms dissolve in the bar corotation region, so that the gas fills this region of the (l, v) diagram approximately evenly and no voids exist.

(ii) Similar voids are visible in the observed ^{12}CO (l, v) diagram. From a comparison with model (l, v) diagrams with different Ω_{sp} but similar Ω_p we find evidence for separate pattern speeds in the Milky Way. The existence of self-consistent models with separate bar and spiral arm pattern speeds was demonstrated by Rautiainen & Salo (1999) in a study of two-dimensional *N*-body simulations, some of which included a massless, dissipative gas component. Models with a growing bar amplitude also support spiral arms in the corotation region (Thielheim & Wolff 1982); however, it is likely that when

self-gravity is included and the spiral arm amplitude becomes nonlinear, the growing spiral pattern will again develop an independent pattern speed.

(iii) From a series of models the preferred range for the bar pattern speed in the MW is $\Omega_p = 60 \pm 5$ Gyr^{-1}, corresponding to corotation at 3.4 ± 0.3 kpc. This agrees well with previous pattern speed determinations by Englmaier & Gerhard (1999), Dehnen (2000) and Debattista et al. (2002). The bar pattern speed is well constrained because it influences not only the inner spiral structure, but also the position of two outer spiral arms in the lv-plot. Models with $\Omega_p = 50$ Gyr^{-1} and $\Omega_p = 70$ Gyr^{-1} are inferior.

The spiral arm pattern speed is less well constrained. Our preferred value is $\Omega_{sp} \approx 20$ Gyr^{-1}, but models with larger $\Omega_{sp} \lesssim \Omega_p$ give only marginally inferior fits to the observed (l, v) diagram.

(iv) Gas flows in models that include massive spiral arms clearly fit the observed ^{12}CO (l, v) plot better than if the potential does not include spiral structure. Furthermore, comparing models with two and four arms in the gravitational potential, we found that only models with four massive arms reproduce the Galactic (l, v) diagram, while gas flows in two-armed potentials do not resemble the spiral arm pattern of the Milky Way.

In Galactic models with four-armed potentials and separate spiral arm pattern speed, the gas flow has two pairs of inner arms that rotate with the bar (lateral and corresponding to the 3-kpc arm) and four outer spiral arms that exhibit a complicated, time-dependent back-and-forth oscillation in the bar frame. The outer and inner spiral structures are connected by a time-dependent transition region around bar corotation.

(v) From a further series of gas models computed for different bar angles, using separately determined luminosity models and gravitational potentials as in Bissantz & Gerhard (2002), we found a range of acceptable bar angles $20^\circ \lesssim \varphi_{bar} \lesssim 25^\circ$. The models for $\varphi_{bar} = 15^\circ$ and 30° are clearly inferior, which is mainly as a result of differences in the inferred gravitational potential.

The model with ($\varphi_{bar} = 20^\circ$, $\Omega_p = 60$ Gyr^{-1}, $\Omega_{sp} = 20$ Gyr^{-1}) gives an excellent fit to the Galactic terminal velocity curve for $10^\circ \leqslant |l| \leqslant 50^\circ$ and to the gaps and spiral arm ridges in the observed CO (l, v) diagram. There are still discrepancies in the bar corotation region where the potential has uncertainties: the 3-kpc arm has too low non-circular velocity, and its counterarm is missing in the data. In the bulge region, closed orbits reproduce the TVC well, while the gas model has lower velocities. This may be a resolution problem in the SPH model, but could in part also be caused by uncertainties in the potential that influence the orbit shapes.

(vi) The 3-kpc arm non-circular velocities can be reproduced by a model in which we artificially increased the $m \geqslant 2$ multipoles of the spiral potential component by 1.5, while keeping all other dynamical parameters fixed. This is well within the uncertainties. Guided by a number of asymmetries in the observed Milky Way gas distribution, we also investigated potentials that are no longer point-symmetric. Some of these models improved the fit to the 3-kpc arm and its counter-arm. Although we did not find a model that at the same time reproduces the entire (l, v) diagram and our standard model, these models suggest that such asymmetries may be important for better understanding the gas flow in the inner Milky Way.

ACKNOWLEDGMENTS

This work was supported by grant 20-64856.01 of the Swiss National Science Foundation.

REFERENCES

Alvarez H., May J., Bronfman L., 1990, ApJ, 348, 495
Amaral L.H., Lépine J.R.D., 1997, MNRAS, 286, 885
Athanassoula E., 1992, MNRAS, 259, 345
Backer D.C., Sramek R.A., 1999, ApJ, 524, 805
Bash F.N., 1981, ApJ, 250, 551
Binney J.J., Gerhard O.E., Stark A.A., Bally J., Uchida K.I., 1991, MNRAS, 252, 210
Binney J.J., Gerhard O.E., Spergel D., 1997, MNRAS, 288, 365
Bissantz N., Gerhard O.E., 2002, MNRAS, 330, 591 (Paper II)
Bronfman L., Nyman L., Thaddeus P., 1989, Lecture Notes in Physics, 331, 140
Burton W.B., Liszt H.S., 1993, A&A, 274, 765
Caswell J.L., Haynes R.F., 1987, A&A, 171, 261
Clemens D.P., 1985, ApJ, 295, 422
Cowie L.L., 1980, ApJ, 236, 868
Dame T.M., Elmegreen B.G., Cohen R.S., Thaddeus P., 1986, ApJ, 305, 892
Dame T.M., Hartmann Dap, Thaddeus P., 2001, ApJ, 547, 792
Debattista V.P., Gerhard O., Sevenster M.N., 2002, MNRAS, 334, 355
Dehnen W., 2000, AJ, 119, 800
Dehnen W., Binney J.J., 1998, MNRAS, 298, 387
Downes D., Wilson T.L., Bieging J., Wink J., 1980, A&AS, 40, 379
Drimmel R., 2000, A&A, 358, 13
Drimmel R., Spergel D.N., 2001, ApJ, 556, 181
Englmaier P., Gerhard O.E., 1997, MNRAS, 287, 57
Englmaier P., Gerhard O.E., 1999, MNRAS, 304, 512 (Paper I)
Feast M.W., Whitelock P., 1997, MNRAS, 291, 683
Fernández D., Figueras F., Torra J., 2001, A&A, 372, 833
Fich M., Blitz L., Stark A.A., 1989, ApJ, 342, 272
Fux R., 1999, A&A, 345, 787
Georgelin Y.M., Georgelin Y.P., 1976, A&A, 49, 57
Grabelsky D.A., Cohen R.S., Bronfman L., Thaddeus P., 1988, ApJ, 331, 181
Hartmann D.A.P., Burton W.B., 1997, Atlas of Galactic Neutral Hydrogen. Cambridge Univ. Press, Cambridge
Hüttemeister S., Dahmen G., Mauersberger R., Henkel C., Wilson T.L., Martin-Pintado J., 1998, A&A, 334, 646
Lépine J.R.D., Mishurov Yu. N., Dedikov S. Yu, 2001, ApJ, 546, 234
Lin C.C., Shu F.H., 1964, ApJ, 140, 646
Lin C.C., Yuan C., Shu F.H., 1969, ApJ, 155, 721
Moriondo G., Giovanardi C., Hunt L.K., 1998, A&A, 339, 409
Ortiz R., Lépine J.R.D., 1993, A&A, 279, 90
Rautiainen P., Salo H., 1999, A&A, 348, 737
Reid M.J., Readhead A.C.S., Vermeulen R.C., Treuhaft R.N., 1999, ApJ, 524, 816
Rix H.-W., Zaritsky D., 1995, ApJ, 447, 82
Sandage A., 1961, The Hubble Atlas of Galaxies. Carnegie Institute of Washington
Sanders D.B., Scoville N.Z., Solomon P.M., 1985, ApJ, 289, 373
Sellwood J.A., Sparke L.S., 1988, MNRAS, 231, 25
Sellwood J.A., Wilkinson A., 1993, Rep. Prog. Phys., 56, 173
Spergel D.N., Malhotra S., Blitz L., 1995, in Minniti D., Rix H.-W., eds, Spiral Galaxies in the Near-IR. Springer, Berlin, p. 128
Stanek K.Z., Mateo M., Udalski A., Szymanski M., Kaluzny J., Kubiak M., 1994, ApJ, 429, 73
Stanek K.Z., Udalski A., Szymanski M., Kaluzny J., Kubiak M., Mateo M., Krzeminski W., 1997, ApJ, 477, 163
Steinmetz M., Müller E., 1993, A&A, 268, 391
Tagger M., Sygnet J.F., Athanassoula E., Pellat R., 1987, ApJ, 318, L43
Taylor J.H., Cordes J.M., 1993, ApJ, 411, 674
Thielheim K.O., Wolff H., 1982, A&A, 108, 206
Vallée J.P., 1995, ApJ, 454, 119
Weiner B.J., Sellwood J.A., 1999, ApJ, 524, 112
Westerhout G., 1957, Bull. AstrI. Neth., 13, 201

This paper has been typeset from a TEX/LATEX file prepared by the author.